Journal of CO_2 Utilization 32 (2019) 92–105

Contents lists available at ScienceDirect

Journal of CO_2 Utilization

journal homepage: www.elsevier.com/locate/jcou

Adsorption of CO_2 gas on graphene–polymer composites

Giulia Magi Meconi[a], Radmila Tomovska[a,c], Ronen Zangi[b,c,*]

[a] POLYMAT & Department of Applied Chemistry, University of the Basque Country UPV/EHU, Avenida de Tolosa 72, 20018 San Sebastian, Spain
[b] POLYMAT & Department of Organic Chemistry I, University of the Basque Country UPV/EHU, Avenida de Tolosa 72, 20018 San Sebastian, Spain
[c] IKERBASQUE, Basque Foundation for Science, Maria Diaz de Haro 3, 48013 Bilbao, Spain

ARTICLE INFO

Keywords:
Molecular-dynamics simulations
CO_2 capture
Graphene
Protic-polymers
Aggregation

ABSTRACT

Three-dimensional graphene-polymer porous materials have been proposed recently as potential adsorbents for carbon dioxide capture. We report results from molecular dynamics simulations on the adsorption of CO_2 gas by composite systems formed by six different types of polymers. All composites are characterized by a constant polymer-to-graphene mass-ratio of 1.02 and their capture capacity as a function of the gas pressure is analyzed relative to the adsorption of nitrogen and methane. The results were then compared to the performance obtained from a bare-graphene sheet. More specifically, we examined the abilities of hydrogen-bond donor groups, amines and amides, as well as aromatic rings to promote and discriminate CO_2 capture. We find that bare-graphene displays the highest capacity to adsorb CO_2. Nevertheless, increasing the number of amine/amide protic groups of the polymer augments the adsorption. In fact, the best performing polymer in our study, which contains three protic groups per monomer, exhibits capture of CO_2 almost as good as bare-graphene. Furthermore, these protic polymers form substantial intra-polymer hydrogen bonds and consequently exhibit cohesive behavior. In these cases, the aggregation of the polymer resulted in partial exposure of the graphene sheet on which the gas can adsorb as well. In contrast aprotic polymers, such as poly(styrene) or poly(methyl-methacrylate), spread extensively on graphene and are characterized by small capacities to adsorb CO_2. For all systems studied, CO_2 is adsorbed preferentially relative to N_2 and CH_4. This preferential adsorption is almost constant as a function of the gas pressure with values ranging from 2 to 12.

1. Introduction

The rapid economic growth of the last century has been accompanied by a dramatic increase in the demand for energy and, as a consequence, by an increase in the use of fossil fuels. The combustion of these fossil fuels, which emits to the atmosphere carbon dioxide (CO_2), is probably the single most important factor in the human influence on climate change [1]. For example in the last sixty years, the concentration of CO_2 in the atmosphere has increased from 314 ppm (parts per million) to a record high level of 409 ppm [2], correlating with an increment of 1.0 °C in the temperature of the earth's surface [3]. Therefore, there is an urgent need to reduce the level of carbon dioxide in the atmosphere.

The challenge of reducing CO_2 emissions has been tackled from different perspectives. These include, improving energy efficiency and conservation, developing clean coal and natural gas technologies [4], and using alternative energy sources such as solar, wind, hydro, and nuclear power [5]. Despite their advantages, all these strategies have limitations which compromise their applications, and as of yet, cannot substantially replace the use of fossil fuel. In fact, fossil fuel is predicted to remain the main source of energy for at least the next two decades [6].

As a short-term solution, CO_2 capture and storage (CCS) is an imperative approach for reducing atmospheric CO_2 concentration. Three different CCS strategies are employed in large-scale production plants: pre-combustion, post-combustion and oxy-fuel combustion. Post-combustion is the most widely used technology because it can be retrofitted into existing power plants. In this case, there are many technologies for separating carbon dioxide from the flue gas stream: solvent absorption, physical adsorption, membrane separation and cryogenic distillation [7–12]. From these methods, solvent absorption with amine is currently the dominant separation approach employed, but it presents various disadvantages, such as amine degradation and the energy required for the absorbent regenerations [1].

In contrast to solvent absorption, a solid sorbent forms only weak physical interactions with CO_2, therefore its regeneration can be easily accomplished by swigging the pressure (PSA) or the temperature (TSA) [13–16]. Large specific surface area, high selectivity and pore structure

* Corresponding author.
E-mail address: r.zangi@ikerbasque.org (R. Zangi).

https://doi.org/10.1016/j.jcou.2019.03.005
Received 13 February 2019; Received in revised form 8 March 2019; Accepted 10 March 2019

are the general characteristics for selecting good solid sorbents. However, the choice of which sorbent material to use depends on the type of combustion strategy (pre-, post- or oxy-fuel combustion) used for the formation of CO_2 [1]. Each strategy creates different conditions (e.g., temperature, pressure, CO_2 content and presence of other type of gases), which influence the carbon dioxide adsorption. For example, in the case of post-combustion the separation of the coal-fired flue gas involves CO_2/N_2, whose pressure is normally at 1 bar and the operating temperature is between 40 °C and 80 °C. In pre-combustion, the separation of CO_2 is from either H_2 or CH_4 at 30 bar and 40 °C [13]. Moreover, the flue gas resulting from post-combustion process contains 10–15% of CO_2, whereas the pre-combustion technology produces a gas mixture composed of the 38% of CO_2 [6]. Obviously, an ideal adsorbent should have good stability and adsorption efficiency under a wide range of process conditions. Currently, typical materials for a solid sorbent include activated carbon, silica, aerogels, zeolites, metal-organic frameworks and porous materials like amine-based sorbents [17,18]. Nonetheless despite the variety of porous solids available, there is a need for better sorbents because they do suffer from several drawbacks: difficulty to handle the solids, slow adsorption rate, low CO_2 selectivity, as well as chemical, thermal and mechanical instability during the processing cycles [6].

Recently, graphene has attracted considerable amount of attention due to its single-atom thickness coupled to impressive thermal, electrical, optical, and mechanical properties [19–22]. It is recognized also as a powerful adsorbent because its electronic structure is responsible for establishing strong London dispersion forces with molecules situated at its surface [23]. More specifically, graphene exhibits a good adsorption strength for CO_2, stronger than for CH_4 and N_2 [24]. A graphene sheet is essentially a two-dimensional (2D) material, and while this geometry offers a large and easily-accessed surface area, the amount of active material per projected area is low. This ratio can be increased substantially by constructing three-dimensional (3D) graphene-based architectures. Such a structure can be obtained by self-assembly of graphene nano-sheets in solution followed by drying-out the aqueous phase [25]. The resulting structure is 3D porous and has been explored in many applications such as batteries, sensors, catalysts, and absorbents [26]. However, adsorption of polymer nanoparticles on the graphene surface was found to be necessary to improve consistency, durability and mechanical resistance [27]. The amount of polymer needed is often determined by trail and error, however, in all cases the polymer does not need to cover the whole graphene exposed area. The resulting graphene–polymer composites are potentially very attractive for CO_2 capture because of the relative simplicity of their re-activation. This is a result of their excellent stability in cycle operations, non-covalent CO_2-graphene interactions, and fast kinetics that allow easy recuperation of the adsorbent [28–32]. Nevertheless, the properties of these graphene–polymer composites depend on the type of polymer adsorbed. Incorporating different functional groups into the polymer can modulate the interaction of the polymer with graphene or with external molecules [27]. It has been demonstrated that the presence of functional groups containing heteroatoms, in particular nitrogen and oxygen, in the polymer composition strengthen CO_2-polymer interaction energy via either dipole-quadrupole or hydrogen-bonding interactions, or both [13]. This strategy has often been exploited to improve the gas sorption of materials for low pressure capture applications, such as those relevant in flue streams and for capture from ambient air [24,33]. We would like to emphasize that these graphene–polymer composites exhibit superior capacity for CO_2 capture relative to, unmodified or chemically-modified, activated-carbon materials [34–36].

In recent years various computational studies addressed the capture of CO_2 gas, alone or in a mixture, by different types of sorbents [37–47]. In this work we perform atomistic molecular dynamics simulations (MD) to investigate the capture of CO_2 gas by several graphene–polymer composite systems and characterize the discrimination with respect to the capture of N_2 and CH_4. Six different types of polymers, with polymer/graphene mass ratio of one, are considered and their performance is compared to that of a bare-graphene system. We find that the adsorption of CO_2 increases with the increase in the number of protic groups in the polymer such as amines and amides. The number of protic groups in the polymer also determine the morphology of the polymer on graphene; those with large numbers tend to self-aggregate whereas those lacking such groups spread homogeneously on the graphene surface. For all graphene–polymer composites, the adsorption of CO_2 is favored relative to N_2 and CH_4.

2. Methods

We performed molecular dynamics simulations to model the adsorption of a mixture of three gases, CO_2, N_2, and CH_4 at graphene–-polymer (GP) composite surfaces. Six different polymers, drawn in Fig. 1, were considered: poly(methyl methacrylate) (PMMA), poly(2-aminoethyl methacrylate) (PEAM), poly(3-diamin-(aminomethyl) propyl methacrylate) (DAPM), poly(aniline methacrylamide) (PAAM), poly(N-(3,5-diaminophenyl)methacrylamide) (PDAFMA), and poly (styrene) (PS). All these polymers are either in common use or expected to provide suitable stability of the graphene material in process cycles [25]. For comparison, we also conducted simulations in the absence of any polymer (referred to as bare-graphene simulations).

A rectangular-shaped box with dimensions of 24.065 nm, 24.668 nm, 64.000 nm, along the *x*-, *y*-, and *z*-axes was used for the simulations. Although, periodic boundary conditions were applied in all three directions, they effectively acted only across the *x*-, and *y*-axes. The simulation box consisted of two non-interacting graphene sheets, periodic in the *xy*-plane, located at $z_1 = 2.0$ nm and $z_2 = 62.0$ nm. In order to prevent translations of the graphene sheets, the positions of their carbon atoms were restrained along the *z*-axis by a harmonic potential with a force constant of 1000 kJ/(mol·nm^2). Each chain of polymer consists of seven monomer units. This length is much smaller than those used in experiments, however, in simulations its advantage is in providing the polymer substantially shorter relaxation times. The difference in the size of the polymer are not expected to influence the strength of the interactions between the composite and the gases, nevertheless, it can affect the adsorbed morphology of the polymer. Equal amount of polymer chains were randomly distributed on both graphene sheets, on the (inner) sides that are facing each other via the larger distance ($z_2 - z_1 = 60.0$ nm). Accordingly, the mixture of gases was placed in that region as well. Experimentally, properties of a GP composite are influenced by the ratio of the polymer mass to that of graphene, m_p/m_G. Therefore, we constructed all systems to have the same polymer/graphene weight ratio, chosen to be equal to 1.020 ± 0.002. Because the size of the graphene sheets were the same in all systems, this meant that the number of polymer chains was different for the different systems (Table 1).

The gas mixture contained equal number of molecules of each gas in the system, $N^o_{CO_2} = N^o_{N_2} = N^o_{CH_4} = \frac{1}{3}N^o_{gas}$. For each type of graphene–polymer system we conducted nine simulations with different numbers of N^o_{gas}. When the system reached equilibrium, we calculated the number of molecules, and from this the density, of each gas in the bulk phase of the simulation box (see Tables S1, S2, and S3). A gas molecule is considered to be in the bulk region if its z-coordinate of its center of mass (com) satisfies, $(z_1 + 4.0\text{ nm}) < z_{gas} < (z_2 - 4.0\text{ nm})$. The distance of 4.0 nm away from the graphene sheet was determined by the onset of a homogeneous (constant) behavior of the density profile for all gases. This bulk density was then used to determine the partial pressure, from the pressure–density curves (see below), each gas exerted on the GP surface. A gas molecules is counted as adsorbed to the graphene sheet if the distance from its com to the graphene com, along the z-axis, is smaller than 0.55 nm. This cutoff value roughly corresponds to the first minimum in the density profiles (see Fig. 6), and captures almost entirely the unimodal distribution of the bare-graphene system. Accordingly, a gas molecule is considered adsorbed to the

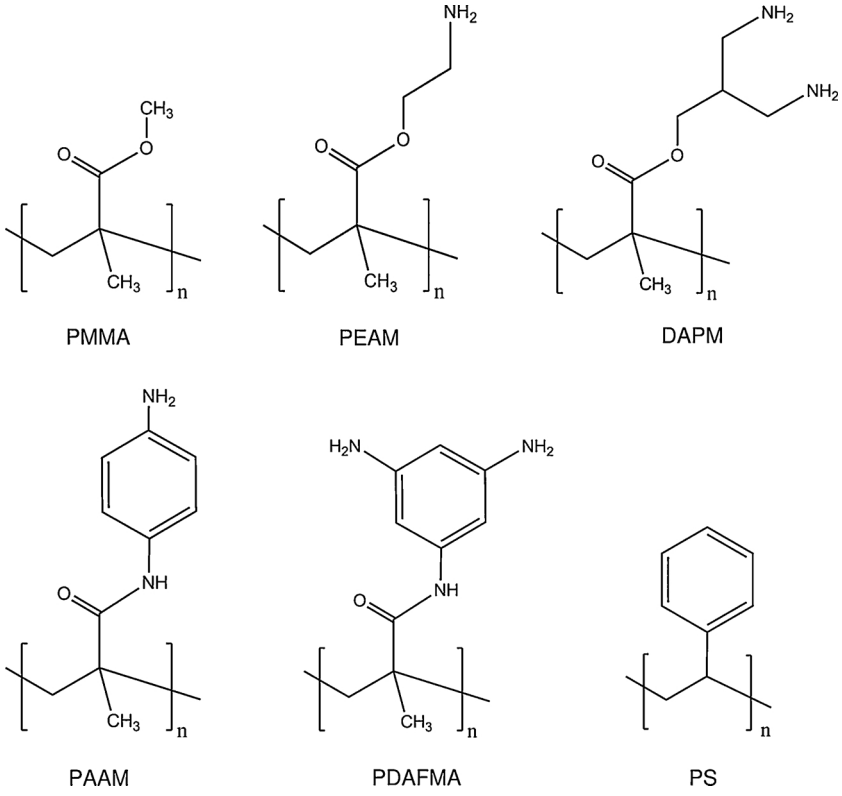

Fig. 1. The chemical structure of the polymers considered in this study. The abbreviated names given correspond to, PMMA: poly(methyl methacrylate), PEAM: poly(2-aminoethyl methacrylate), DAPM: poly(3-diamin-(aminomethyl)propyl methacrylate), PAAM: poly(aniline methacrylamide), PDAFMA: poly(N-(3,5-diaminophenyl)methacrylamide), and PS: poly(styrene).

Table 1
The number of chains of each polymer (each chain contains seven monomer units), their total mass, m_p, and the polymer/graphene mass ratio, m_p/m_G, which is designed to be constant for all systems. In all simulations, including those with bare graphene, the number of carbon atoms of the two graphene sheets is 45472 corresponding to a mass of 9.070×10^{-19} g.

Polymer	N_{chains}	m_p [10^{-19} g]	m_p/m_G
PMMA	808	9.242	1.019
PEAM	624	9.244	1.019
DAPM	492	9.264	1.021
PAAM	480	9.257	1.021
PDAFMA	420	9.252	1.020
PS	760	9.234	1.018

polymer if the distance from its com to any atom of the polymer is smaller than 0.55 nm. The amount of gas molecules adsorbed at the GP composite surface is expressed by its two-dimensional mass density, $\rho_{2D} = m/A$, where m is the mass of the adsorbed gas and A is the area of the two graphene sheets. Two molecules were considered to be hydrogen bonded if the donor–acceptor distance is smaller than 0.35 nm and the hydrogen–donor–acceptor interaction angle is smaller than 30° [48]. Figure S1 displays a snapshot of the entire simulation box of one of the G-PDAFMA systems.

All simulations were performed in the canonical ensemble (NVT) using the molecular dynamics package GROMACS version 4.6.5 [49]. The simulation box was fixed during the simulations and a constant temperature of 300 K was maintained by the velocity rescaling thermostat [50] with a coupling time of 0.1 ps. The time step for integrating the equations of motion was set to 2 fs. Bonds stretching and angles bending were described by harmonic potentials. Lennard–Jones (LJ) interactions between unlike atoms were computed using the geometric combination rules of the OPLSAA force-field. The GP composite systems were subjected to a relaxation time of 40 ns, except those with $N^o_{gas} = 2700$ where the equilibration time was extended to 60 ns. Due to absence of polymer chains in the bare-graphene system, these simulations reached equilibrium much faster and therefore the relaxation time was shortened to 30 ns. Then, all simulations were continued for additional 10 ns of data collection. Figure S2 displays the convergence properties of the G-PAAM system examined by the density profiles along the z-axis of the polymer and CO_2 gas molecules.

Table 2
The non-bonded parameters for the models of carbon dioxide and nitrogen gases.

	$q[e]$	σ [nm]	ϵ [kJ/mol]
C (CO_2)	+0.70	0.280	0.224
O (CO_2)	−0.35	0.305	0.657
N (N_2)	−0.482	0.3318	0.303
MW (N_2)	+0.964	0.0000	0.000

2.1. Interactions parameters

A carbon dioxide molecule was represented by the TraPPE model [51] for which the non-bonded interactions are specified in Table 2.

In this case, the Lorentz–Berthelot combination rules were used. The carbon-oxygen covalent bond [52] is 0.116 nm long with a force constant of 476976 kJ/(mol· nm^2). We adopted a force constant of 1236 kJ/(mol·rad^2) for the linear O–C–O bond angle from the EPM2 model [53]. The three-site model of Murthy et al. [54] was utilized to describe a nitrogen molecule (see Table 2). In this model, a positively-charged massless virtual site (MW) is symmetrically placed between the two nitrogen atoms. The covalent bond between the two nitrogens is characterized by an equilibrium distance of 0.1098 nm and a force constant [55] of 138570 kJ/(mol·nm^2). A methane molecule was represented by the OPLSAA force-field [56]. To validate the force-fields described above for CO_2, N_2, and CH_4 gases we performed a series of MD simulations in the NVT ensemble, modeling the homogeneous gas phase, for each of these gases. Seven different densities were considered for which the pressure was calculated and compared against experimental data [55] obtained from the van der Waals equation of state (see Table S4).

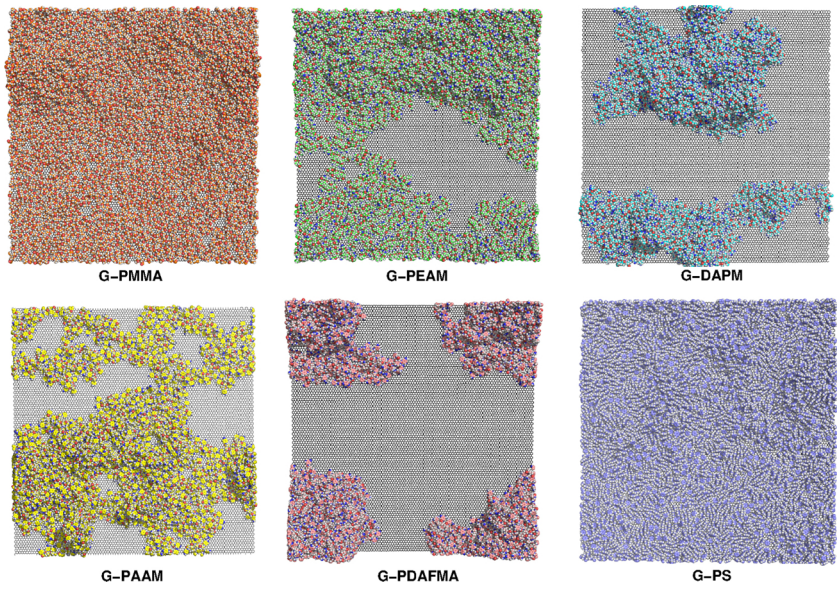

Fig. 2. Snapshots of the structural organization of the different polymers on the graphene sheet. The figures display top-views, of the last configuration, on one of the two graphene–polymer interfaces taken from simulations with a partial pressure of CO_2 at, approximately, 1 bar. For clarity, none of the gas molecules present in the system are displayed. Graphene is shown as black sticks. Polymers are represented as spheres, where hydrogens are colored in white, oxygens in red and nitrogens in blue. Carbon atoms have different colors in each polymer (orange for PMMA, green for PEAM, cyan for DAPM, yellow for PAAM, pink for PDAFMA, and violet for PS).

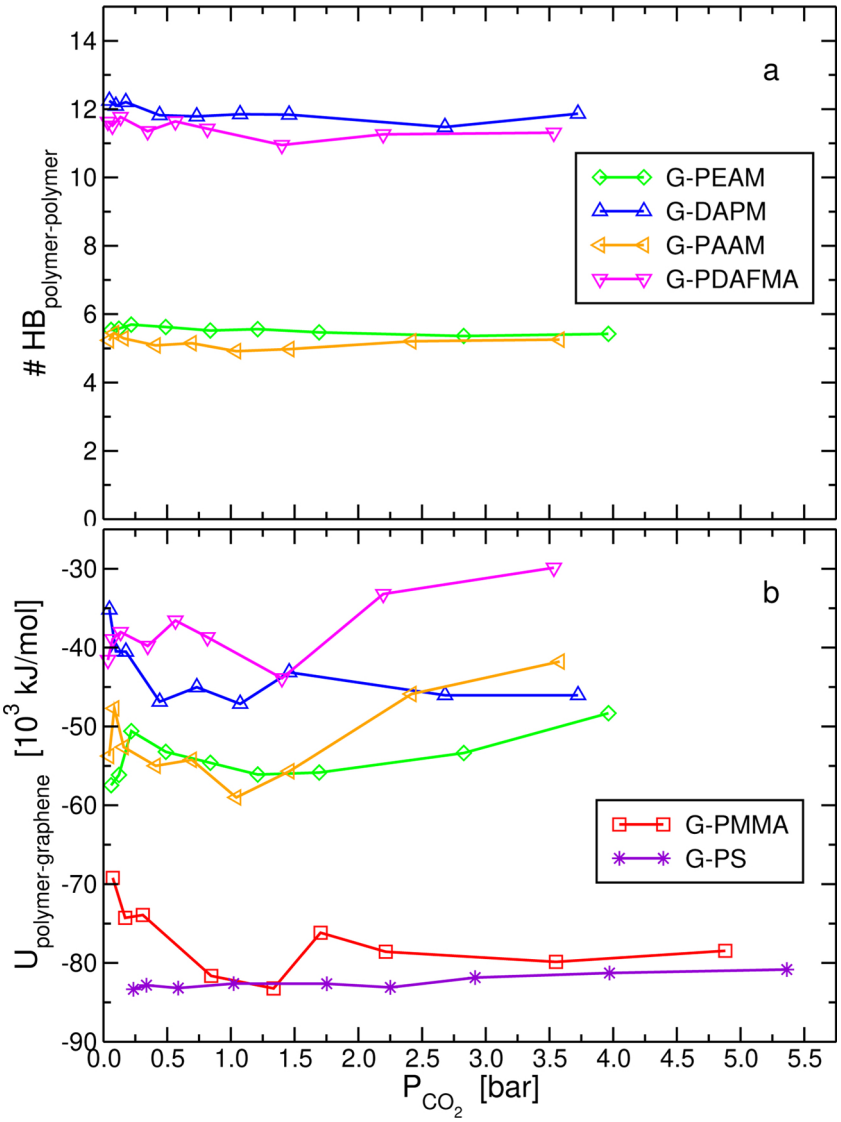

Fig. 3. (a) The number of polymer–polymer hydrogen bonds, per polymer molecule, and (b) the potential energy between the polymer and the graphene sheet, as a function of the partial pressure of CO_2.

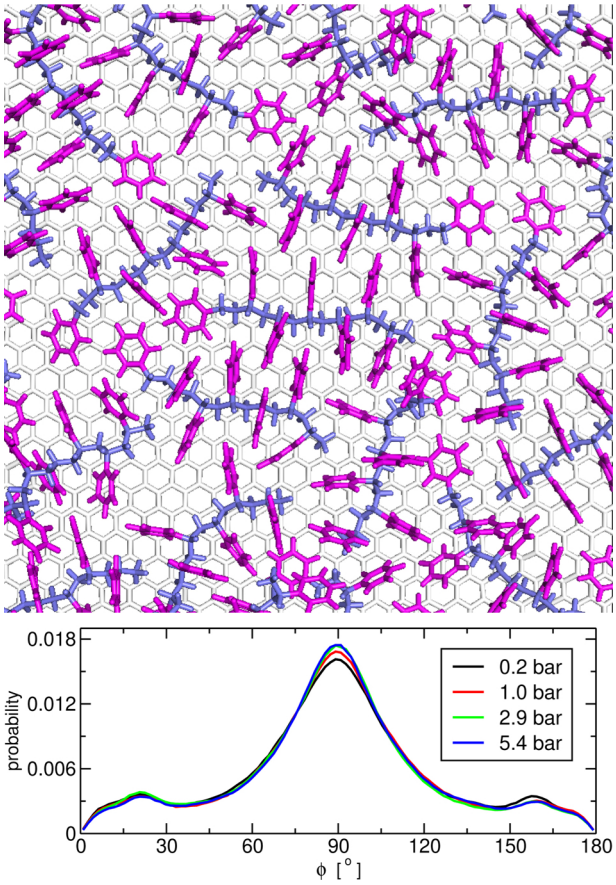

Fig. 4. Top panel: top-view of the poly(styrene) chains on graphene. The phenyl rings are colored in magenta and the backbones in blue. For clarity, all gas molecules were removed from the figure. Lower panel: normalized distribution of the angle, ϕ, between the plane of the phenyl ring and the z-plane, at four different partial pressures of CO_2.

The results, which are shown in Fig. S3, indicate these models reasonably predict the gas pressure, albeit consistently underestimating its value.

Details of the parameters used to model the flexible graphene sheets (thus including bond stretching and angle bending) are described in a previous simulation study [57], in which the LJ parameters of the carbon atoms, σ_{CC} = 0.3851 nm and ϵ_{CC} = 0.4396 kJ/mol, were parameterized to mimic single-walled carbon nanotubes [58]. The model for PS, taken from our previous work [59], together with the models of the other polymers, constructed for this study, are specified in the Supplementary Material.

3. Results and discussion

First we examine the morphologies formed by the different polymers when adsorbed on the graphene sheet. Top-view snapshots of the composite systems are shown in Fig. 2. PS and PMMA cover completely, or almost completely, the graphene sheet. In contrast, the other graphene–polymer composites display different degrees of aggregation of the polymer. From this point of view, the polymers can be grouped into those with moderate degree of aggregation (PEAM and PAAM) and those with strong degree of aggregation (DAPM and PDAFMA). The extent of aggregation is a result of the interaction energy between the polymer chains relative to the interaction between the polymer and graphene. Not surprisingly, each of the monomers of PEAM and PAAM contains one amine group whereas those of DAPM and PDAFMA contain two amine groups. These amine groups are able to form hydrogen bonds with one another which strengthen the polymer–polymer attraction at the expense of the lost polymer–graphene energy, a process accompanying the course of aggregation. Note that the amide groups of the polymer play a minor role in the polymer–polymer hydrogen bonds because of their proximity to the backbone chain. We calculate the number of hydrogen bonds formed between and within the polymer chains in Fig. 3a. The above mentioned grouping of the polymers (according to their degree of aggregation) is apparent in this figure as well. Because PS and PMMA do not contain suitable groups for hydrogen bond formation their corresponding values are zero by definition. DAPM and PDAFMA form similar numbers of intra-polymer hydrogen bonds which are about twice as much as those formed by PEAM and PAAM. Obviously, larger numbers of hydrogen bonds within the polymer strengthen the polymer–polymer interaction energy and will induce aggregation and intrusion into the gas bulk phase. As a consequence, the strength of the interaction of the polymer with the graphene sheet will display the inverse order, as found in Fig. 3b. PS and PMMA have the strongest adsorption energy with graphene whereas PDAFMA and DAPM display the weakest adsorption, a trend that correlates well with the formed morphologies shown in Fig. 2. It is worth noting that in PS the phenyl aromatic rings are oriented perpendicular to the graphene sheet as the backbone chains lie flat on the surface. This is shown in a snapshot in Fig. 4 and by the distribution of the angle between the plane of the phenyl ring and the graphene's plane. The distribution has a pronounced maximum at 90° and small maxima at 20° and 160°. The latter two maxima result because the first phenyl in the chain is able to orient almost parallel to the surface.

The ability of the proposed graphene–polymer composite surfaces to capture CO_2 gas at 300 K is shown in Fig. 5. In Fig. 5a this is expressed by the two-dimensional mass-density of adsorbed CO_2, averaged over the two composite surfaces in the simulation box, as a function of its partial pressure. These adsorption isotherms indicate that bare-graphene has the highest capability to adsorb CO_2, slightly better than the best performing graphene–polymer composite system, G-PDAFMA. The other graphene–polymer systems exhibit the following decreasing order of performance in adsorbing CO_2 gas: G-PAAM > G-DAPM > G-PEAM > G-PMMA > G-PS. The percentage of CO_2 molecules adsorbed at the surfaces relative to the total number of CO_2 molecules is shown in Fig. 5b. This percentage ranges from 83% to 18% and decreases substantially with the increase in the partial pressure. The latter is manifestation of interactions between the adsorbed molecules. Nevertheless for the G-PS system, which exhibits the lowest ability to adsorb CO_2, the decrease is very mild. In this case, the adsorption isotherm is almost linear and is analogous to Henry's law of the amount of gas dissolved in a liquid.

In order to investigate the way CO_2 molecules are adsorbed at the graphene–polymer surfaces, we plot in Fig. 6 the density profile of the CO_2 molecules along the z-axis (normal to the graphene sheet) for systems with $N^o_{CO_2}$ = 2700 yielding partial pressures in the range of 1–2 bar. Except for G-PS and G-PMMA, the first peak away from the graphene sheet is by far the most dominant. For bare-graphene, the distribution is unimodal indicating the formation of only monolayers. This is also true for bare-graphene systems with larger numbers, or higher partial pressures, of CO_2 (profiles not shown). The location of this first peak, 0.35 nm away from the average positions of the carbon atoms of graphene, points to van der Waals contacts. For the graphene–polymer systems, there is a second peak which is broad and for some systems there is even a third peak or a shoulder at distances 0.70–0.96 nm away from graphene. For G-PS the integral of the second and third peaks is significantly larger than that of the first peak, whereas for G-PMMA these integrals are comparable. These second and third peaks originate due to adsorption of CO_2 either inside (i.e. absorption) or at the outer surface of the polymer and are not an indication of multilayer formation of adsorbed CO_2 even at the highest gas pressure studied. The systems with the added polymer exhibit also a slow decay of the CO_2 density along the z-axis and only at around 4.0 nm away from the graphene sheets, does the density adopt a constant value characterizing the 'bulk-

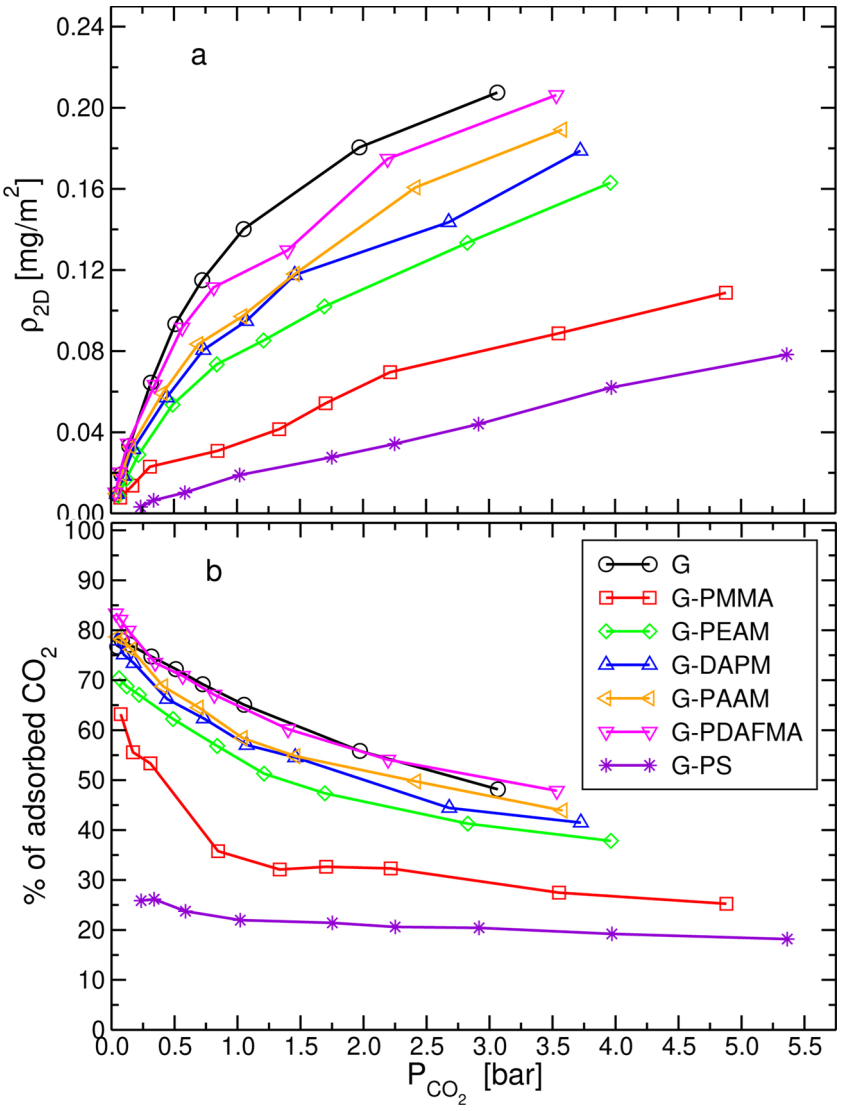

Fig. 5. Adsorption isotherms of CO_2 gas on graphene–polymer composite surfaces, as well as for bare graphene sheet, at 300 K. (a) The two-dimensional density of the CO_2 gas adsorbed. (b) The percentage of the number of CO_2 molecules adsorbed at the surface relative to the total number of CO_2 in the system. Both graphs are plotted as a function of the partial pressure of CO_2 in the system.

region' in the simulation box. This slow decay results from the adsorption to the polymer and its range coincides with the extent of polymer intrusion into the gas phase.

Thus, the CO_2 molecules are adsorbed to the graphene sheet as well as to the chains of the polymer. Nevertheless, although the adsorption to the graphene and the polymer can be done independently, CO_2 molecules are also adsorbed simultaneously to both. In Fig. 7 we display a snapshot of the graphene–polymer interface isolating six CO_2 molecules that exhibit the three different adsorption modes. Adsorption only-to-graphene, as well as, simultaneous adsorption to graphene and polymer give rise to the first peaks in Fig. 6. In the latter the polymer covers the adsorbed molecules, thereby, increasing the adsorption energy and at the same time reducing the graphene–polymer attraction. In the adsorption only-to-polymer, the gas molecules are adsorbed at the surface of, or absorbed inside, the polymer. The population of each adsorption mode is plotted in Fig. 8 which demonstrates there is a large difference between the adsorption mechanism of G-PS and G-PMMA to that of the other graphene–polymer systems. G-PS displays a negligible adsorption via the only-to-graphene mode for all partial pressures of CO_2. For G-PMMA, there is a sharp decrease in the adsorption of only-to-graphene, after which the contribution of this adsorption mode is also negligible. This behavior of the G-PS and G-PMMA systems arises because these polymers spread extensively on the graphene sheet (Fig. 2). Consequently for these two polymer systems, the largest contribution for CO_2 adsorption comes from the only-to-polymer mode. For the other graphene-polymer composite systems, all three adsorption modes contribute substantially. In most cases, the only-to-graphene mode has the largest contribution. The other two adsorption modes are more or less comparable in their populations, where the only-to-polymer and the simultaneous adsorption modes slightly increases and slightly decreases, respectively, with the partial pressure.

As it was shown above, the density of the amine groups of the polymer chains influences the morphology of the assembly on the graphene sheet. However, the main purpose for introducing this group is its potential ability to form hydrogen bonds with the CO_2 molecules. In Fig. 9a we present the number of hydrogen bonds the polymer forms with carbon dioxide. The graph indicates that the larger the number of these hydrogen bonds the larger the capacity of the graphene–polymer composite systems to capture CO_2 gas as calculated in Fig. 5. For the polymers considered in this study, larger number of amine groups resulted in more hydrogen bonds. Note that PAAM and PDAFMA contain also amides groups capable of donating and accepting hydrogen bonds. In fact, the contribution of these amide groups to the total number of hydrogen bonds formed between the polymer and the CO_2 molecules is

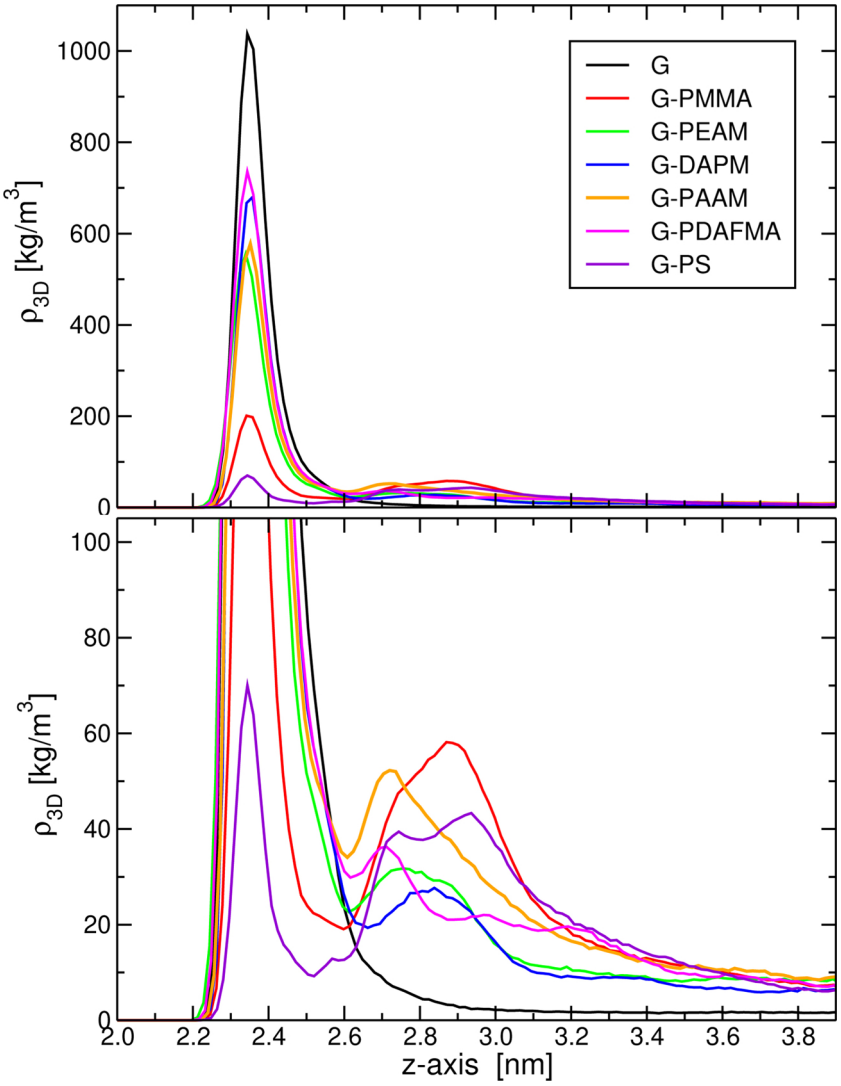

Fig. 6. Upper panel: The density profile of the CO_2 molecules along the z-axis for different graphene–polymer composite systems with $N^{o}_{CO_2} = 2700$. These profiles were averaged over the two surfaces in the simulation box by folding the center of mass of the second graphene sheet (at $z_2 = 62.0$ nm) onto the first one at $z_1 = 2.0$ nm. Lower panel: A zoom-in of the density profiles displaying the second peaks due to adsorption to the polymers.

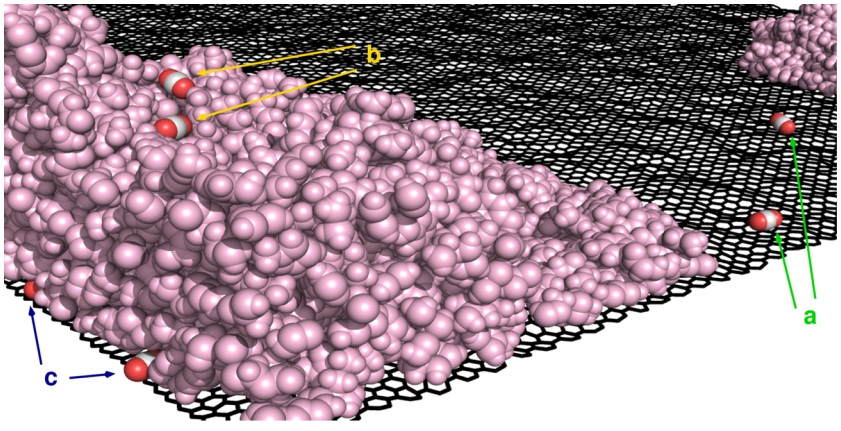

Fig. 7. A snapshot of a segment of the simulation box for the graphene-PDAFMA composite system displaying three different types of adsorption of CO_2 gas at the interface. Adsorption only to the graphene sheet (a), only to the polymer (b), and simultaneously to the graphene and the polymer (c). The graphene sheet is shown as black rods, the polymer atoms as pink spheres, and the carbon dioxide molecules as white and red spheres. For clarity, nitrogen and methane gases, as well as other CO_2 molecules, were removed.

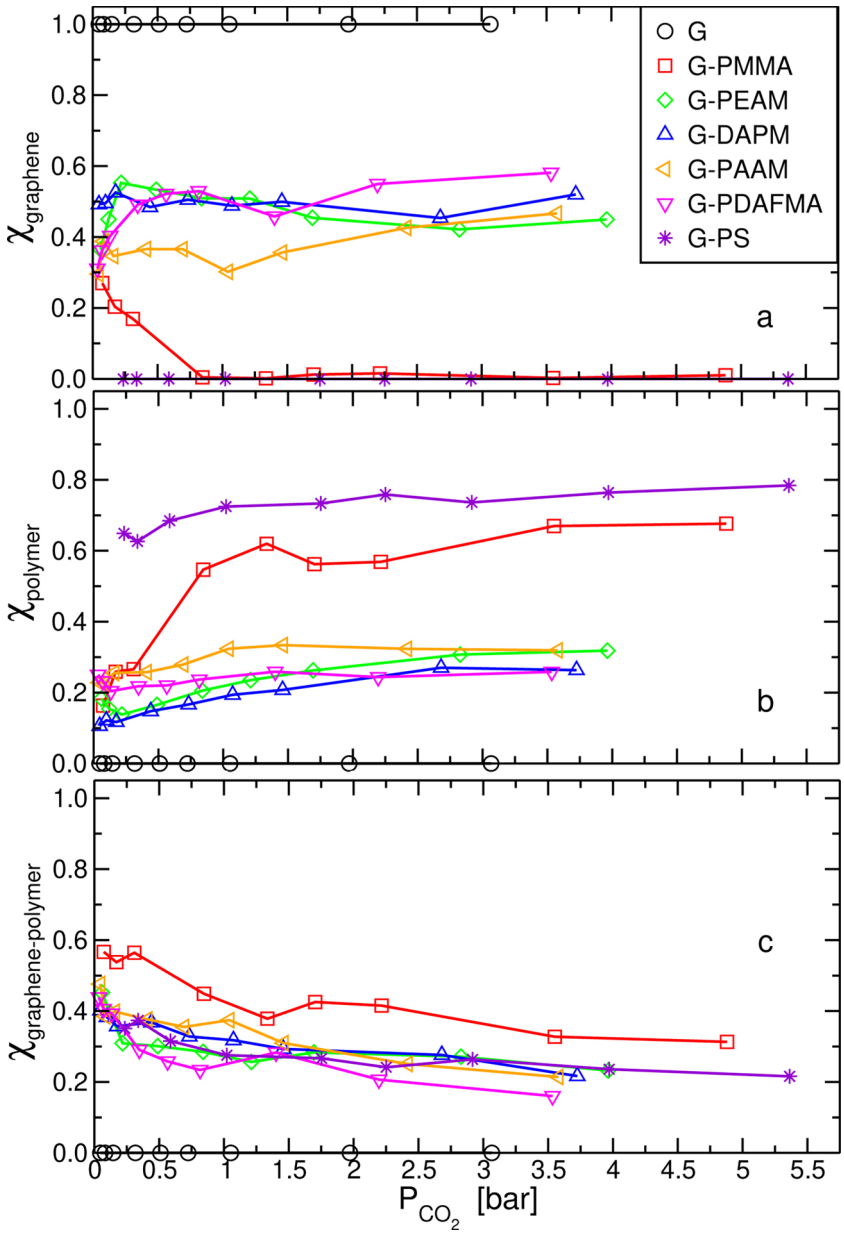

Fig. 8. The decomposition of the adsorbed CO_2 molecules into the different modes of adsorption. The graphs exhibit the fraction of carbon dioxide molecules adsorbed (a) only to the graphene sheet, (b) only to the polymer, and (c) simultaneously to the graphene and the polymer, relative to the total number of CO_2 adsorbed.

significant (see Fig. S4). Thus the amine and amide groups, both, augment the capture of CO_2 gas, the latter by direct interactions, whereas the former also by aggregation, exposing areas of bare-graphene that relative to the graphene–polymer models considered here exhibit the highest performance in adsorbing CO_2 gas. As expected, the curves in Fig. 9a show saturation behavior at higher pressures because of a decrease in available hydrogen bond donors. In Fig. 9b, we display the ratio of the number of hydrogen bonds to the number of CO_2 molecules adsorbed only to the polymer. This ratio is larger than one for G-PDAFMA and G-DAPM at low pressures because one CO_2 molecule can form two (or theoretically more) hydrogen bonds to the amine groups of the polymer. At these low partial pressures, it is evident that the adsorption to the polymer via a hydrogen bond(s) is the predominant mechanism for all systems. As the partial pressure of CO_2 increases, the extent of adsorption by nonspecific dispersion interactions increases as well, again because of saturating the hydrogen donor sites. Fig. 10 displays three snapshots from the simulation of G-PDAFMA system depicting an adsorbed carbon dioxide molecule forming two, one, and zero hydrogen bonds.

As mentioned in the Methods section, in all systems the carbon dioxide gas is placed together with nitrogen (N_2) and methane (CH_4) gases, all with equal number of molecules. This is because optimized removal of CO_2 has to discriminate the binding to this gas with respect to binding other gases present in the air to be purified. Nitrogen is naturally present in the atmosphere in a large quantity and methane is one of the products of fuel combustion. Fig. 11 displays the percentage

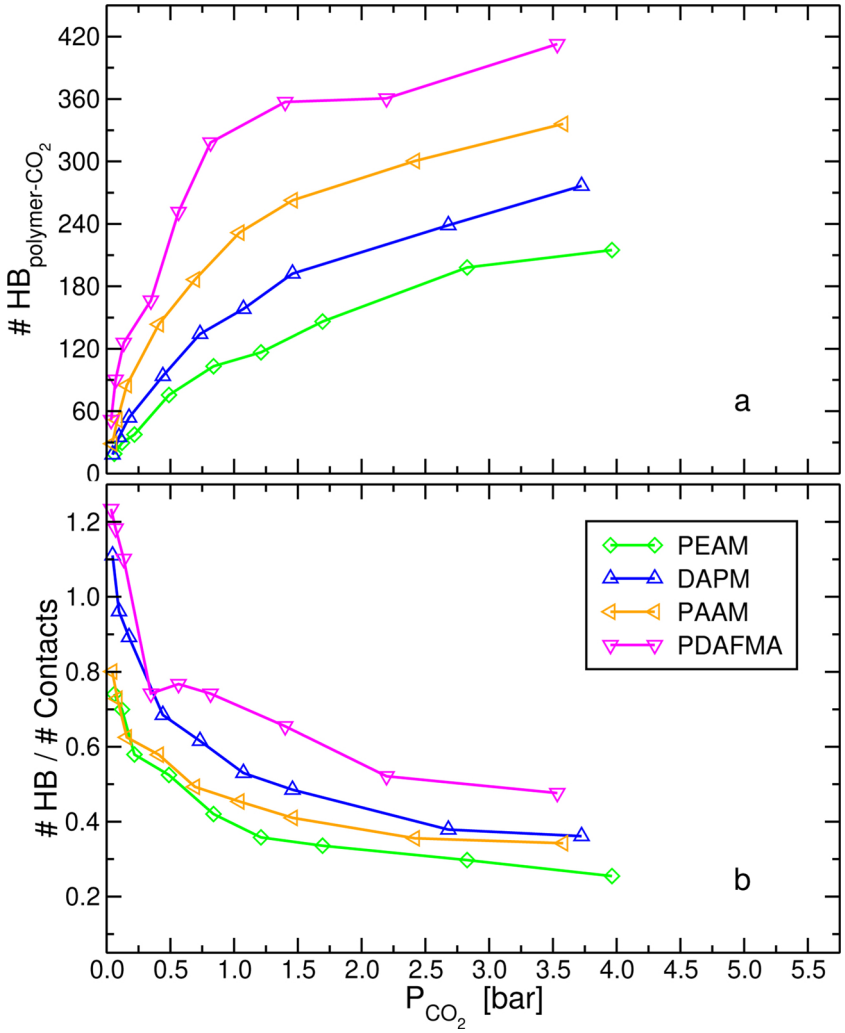

Fig. 9. The number of hydrogen bonds between the polymer and CO_2 molecules. (a) Absolute numbers, and (b) the ratio relative to the number adsorbed by the only-to-polymer mode, as a function of the partial pressure of CO_2.

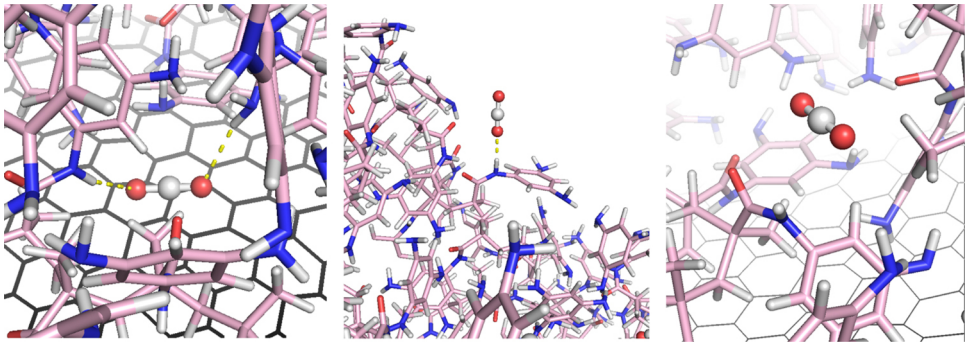

Fig. 10. Snapshots from the simulation of the G-PDAFMA composite system showing a CO_2 molecule in a ball and stick representation that is: (left) bound simultaneously to graphene and polymer and forms two hydrogen bonds, (middle) bound at the air/polymer interface and forms one hydrogen bond, (right) absorbed inside the polymer by nonspecific interactions (zero hydrogen bonds).

of the adsorbed molecules for these two gases as a function of the partial pressure of each gas. In these cases the amounts of gases adsorbed are smaller than in the case for CO_2, ranging from 55% down to 15%. Again, the constant values exhibited by G-PS, and by G-PMMA above 1 bar, indicate the adsorbate molecules behave ideally and do not interact with one another. The decrease exhibited by the G-PMMA system up to around 1 bar is because at very low pressures the adsorption due to only-to-graphene mode saturates very quickly. This is because in this system the area of exposed graphene is very small. Once the binding sites on the exposed graphene are saturated, there is an onset of adsorption only to the polymer (a similar behavior occurs for the adsorption of CO_2 shown in Fig. 5b and explained by the changes of the different adsorption modes shown in Fig. 8). In Fig. 12 we calculate the selectivities of the adsorption. We adopt the formalism of

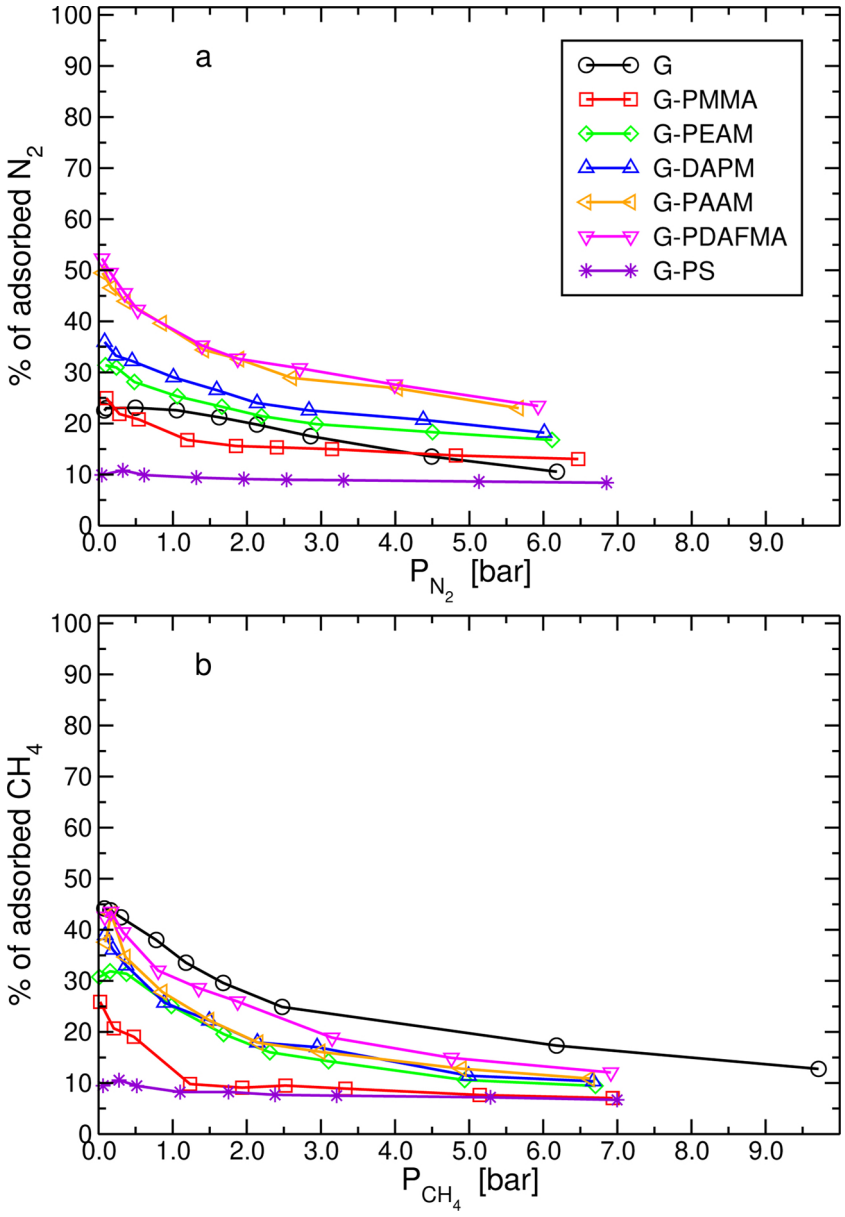

Fig. 11. The adsorption of the other two gases in the system. The figure displays the percentage of the number of gas molecules adsorbed at the graphene–polymer composite surface relative to the total number of these gas molecules in the system, plotted as a function of the partial pressure of the gas. (a) For nitrogen and (b) for methane.

preferential binding [60] and plot the excess number of CO_2 molecules adsorbed to the graphene–polymer composite, ν'_{CO_2}, by

$$\nu'_{CO_2}(x) = \frac{\theta_{CO_2}\ N_x}{\theta_x\ N_{CO_2}} \tag{1}$$

where θ_i is the number of molecules of gas i adsorbed to the composite. These numbers of adsorbed gas molecules are then divided by the corresponding numbers in bulk, N_i, to yield a measure of the excess ($\nu'_{CO_2} > 1$) or depleted ($\nu'_{CO_2} < 1$) number of adsorbed CO_2 molecules relative to a random distribution, i.e., relative to the number that would be observed if there was no preference in binding of the two gases to the composite ($\nu'_{CO_2} = 1$). The results are shown in Fig. 12 with respect to (a) x = N_2 and (b) x = CH_4. For all graphene–polymer composites, CO_2 gas is adsorbed preferentially relative to nitrogen and methane. The curves are more or less constant as a function of the amount of gas in the system with values ranging from 2 to 7. This constant behavior is expected. If u_{GP-i} is the interaction energy between the composite and gas i, per gas molecule, and μ_i^0 is the standard chemical potential of gas i, then it can be shown [61] that,

$$\ln \nu'_{CO_2}(x) = \beta(\mu^0_{CO_2} - \mu^0_x) \ln \frac{\mathcal{Z}'_{CO_2,ads}}{\mathcal{Z}'_{x,ads}} + \beta(u_{GP-CO_2} - u_{GP-x}) \tag{2}$$

where $\mathcal{Z}'_{i,ads}$ is the single-site molecular partition function, summed over internal energies, of adsorbate i, and β is $1/k_BT$. Thus, the preferential adsorption of CO_2 is independent of N^o_{gas}.

Nevertheless, there are some deviations from a constant behavior, especially for the bare-graphene system. Although, we did not evaluate the first term on the right-hand side of Eq. (2), we attribute these

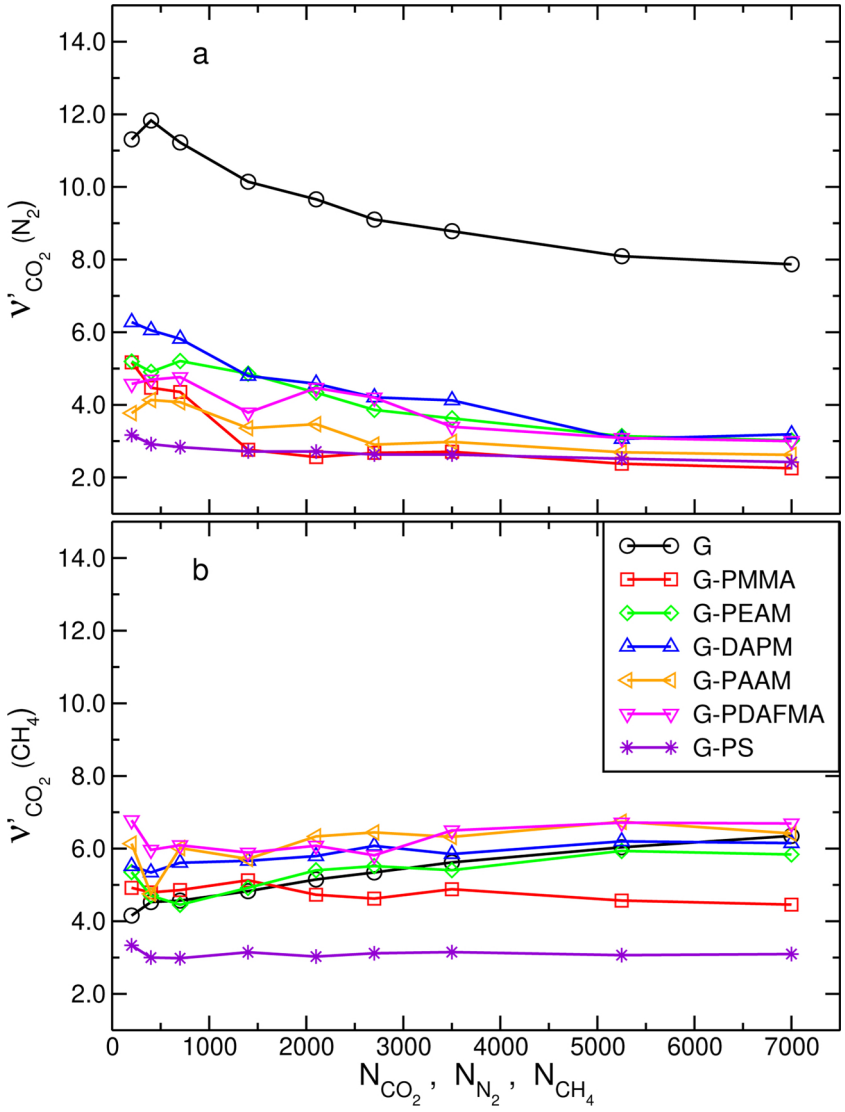

Fig. 12. The selectivity of the graphene–polymer composite surface to adsorb CO_2 relative to the adsorption of (a) nitrogen and (b) methane at 300 K. These selectivities are expressed as the ratio of the number of molecules of the two gases adsorbed at the interface divided by the corresponding ratio in bulk (see Eq. (1)) and plotted against the number of molecules of each gas in the system ($N_{CO_2} = N_{N_2} = N_{CH_4}$).

deviations for the breakdown of the non-interacting adsorbing-sites approximation on bare-graphene [62]. In fact, as the pressure increases, there are increasing interactions between the adsorbate molecules which ultimately form clusters. Fig. 13 displays the probability distribution of forming clusters of different sizes for the three gases. CO_2 has the highest probabilities to form clusters and it also forms clusters with sizes much larger than N_2 and CH_4. A snapshot representing this behavior of carbon dioxide on bare-graphene for the system with the densest gas is shown in Fig. 14. We argue, that the reason adsorbed CO_2 molecules display extensive clustering relative to the other two gases is because they are characterized by a large quadrupole moment and with a proper arrangement on a two-dimensional surface, they can interact favorably with one another via electrostatic interactions. Note that the electric quadrupole moment for methane is zero and for nitrogen is about a third of that of carbon dioxide [63].

Fig. 12 indicates that the preferential adsorption of CO_2 on bare-graphene relative to N_2 is much larger than that relative to CH_4. We calculated u_{GP-i} by energy minimization of a single gas molecule on a graphene sheet and found it to be, 25.1, 13.3, and 16.5 kJ/mol for i = CO_2, N_2, and CH_4, respectively. Thus qualitatively, the preferential adsorption correlate with the binding energies. We can then calculate the undetermined term $\beta(\mu^0_{CO_2} - \mu^0_x) \ln \frac{\mathcal{Z}_{CO_2,ads}}{\mathcal{Z}_{x,ads}}$ in Eq. (2) and obtain -2.3 and -2.0 for the relations involving N_2, and CH_4, which are very similar values. Thus for these gases on bare-graphene, the changes in preferential adsorption is predominantly determined by the different binding energies. For the systems with the polymers, the binding energies and the molecular partition functions of the adsorbed gas need to be calculated for each adsorption mode (Fig. 8) separately, thereby, impeding easy evaluation of the preferential adsorption.

4. Conclusions

Three-dimensional porous material made by self-assembly of graphene sheet can be a very good adsorbent for the capture of CO_2.

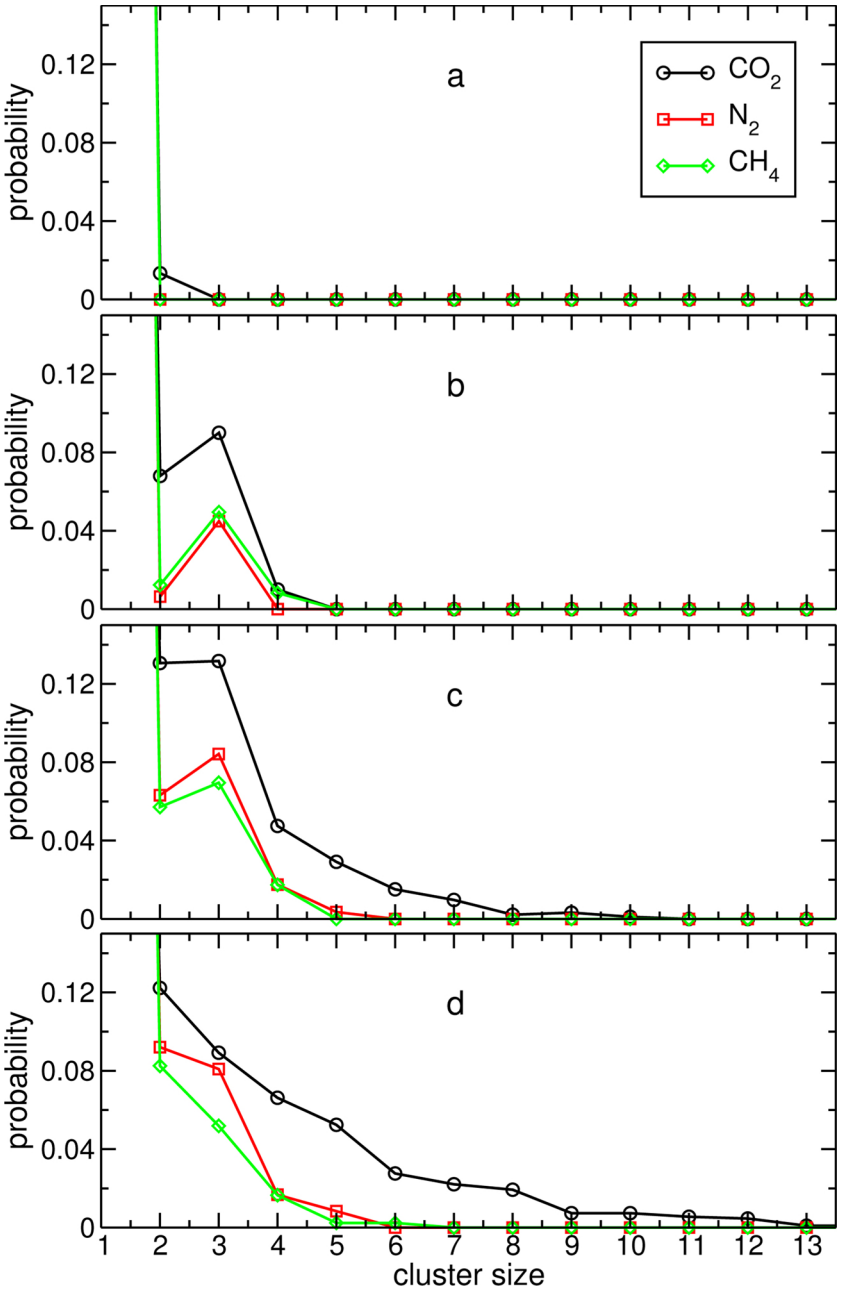

Fig. 13. Normalized distributions of the size of clusters formed by gas molecules adsorbed on graphene (for the simulations with bare-graphene) at four different bulk gas densities, spanning the whole range of pressures. More specifically, the analysis was performed for the simulations with (a) 200, (b) 1400, (c) 3500, and (d) 7000, molecules of each gas (see Tables S1–S3). Two molecules are considered bound to each other if their distance between their centers of mass is smaller than 0.5 nm (which is around the first minimum in the corresponding radial distribution functions). Note that at low densities, the majority of the molecules do not form clusters (cluster-size = 1).

However, improved mechanical properties of this porous structure require the presence of polymer latex generating a graphene–polymer composite material. In this paper we investigated, from a physicochemical point of view, several polymers to generate such composite systems that maximize the capacity to adsorb CO_2 molecules. Furthermore, the ability of the composite materials to discriminate against the binding of potentially competing gases, N_2 and CH_4, is examined as well. We address these questions by all-atom molecular dynamic simulations in the canonical ensemble. In this case, the composite material is in direct equilibrium with the gas mixture which consist of equal number of CO_2, N_2 and CH_4 molecules. Obviously, a strong binding energy between the polymer and CO_2 will favor the adsorption. For this reason, we consider the incorporation of protic groups into the polymer such as amines and amides. In addition, a benzene ring can interact favorably with CO_2 due to dispersion interactions and therefore its incorporation into the proposed polymers was tested as well. The performance of the graphene–polymer systems was compared with those of bare-graphene which actually exhibited the best capacity to adsorb CO_2 molecules. Nevertheless, the graphene–polymer system that performed the best was only slightly below that of bare-graphene.

Despite the fact that for all systems, the ratio between the mass of the polymer to that of the graphene sheet was constant, the different polymers considered adsorbed onto the graphene sheet with different morphologies. The main factor determining the assembled structure was the number of protic groups of the polymer. The larger the number of these groups, the stronger the cohesive forces (due to intra-polymer hydrogen bonds) and the stronger the aggregation. As a consequence, there is a partial exposure of graphene on which the gas can adsorb as

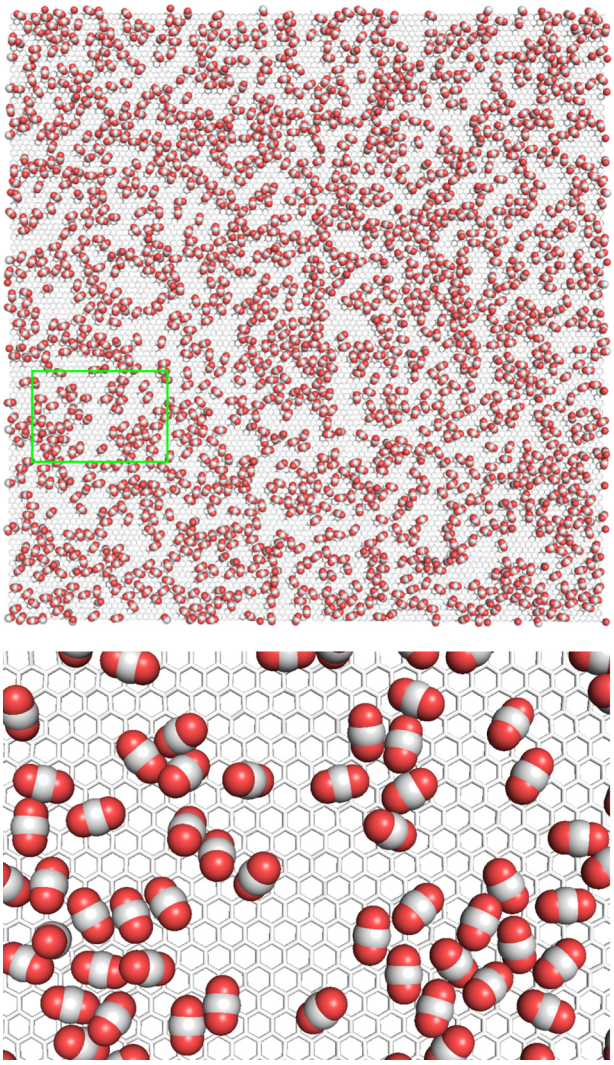

Fig. 14. Upper panel: a snapshot of the arrangement of CO_2 molecules adsorbed on one of the graphene sheets for the simulation of bare-graphene at the highest partial pressure of CO_2 (7000 gas molecules). Lower panel: magnification of the green boxed-area above. For clarity, nitrogen and methane molecules are now shown.

well. Such behavior of the graphene–polymer system induces three types of adsorption modes, whose relative populations depend on the properties of the polymer.

We find that aprotic polymers capture the lowest amount of CO_2. This is because these polymers 'wet' very well the surface of graphene and their dispersion interaction with CO_2 is relatively weak. In contrast, composites with protic polymers perform better and the adsorption of CO_2 increases with the number of protic groups (such amines and amides) in the polymer. This is in agreement with recent experimental results on the capture of CO_2 by amine infused hydrogels [64]. The contribution of hydrogen bonds to bind CO_2 to the polymer is very high at low pressures and decreases with increasing the gas pressure while nonspecific interactions become increasingly more abundant. For all systems considered in the simulations, CO_2 binds to the adsorbent in excess relative to N_2 and CH_4. Above a critical gas pressure in the bare-graphene system, the adsorption of CO_2 molecules involves formation of clusters whose size and population increase with the pressure.

Acknowledgments

This work was supported by a grant from the ministry of economy and competitiveness of the Spanish government, reference number CTQ2016-80886-R. We would like to thank the technical and human support of the computer cluster provided by IZO-SGI SGIker of UPV/EHU and European funding (ERDF and ESF).

Appendix A. Supplementary Data

Supplementary data associated with this article can be found, in the online version, at https://doi.org/10.1016/j.jcou.2019.03.005.

References

[1] D.Y. Leung, G. Caramanna, M.M. Maroto-Valer, An overview of current status of carbon dioxide capture and storage technologies, Renew. Sust. Energ. Rev. 39 (2014) 426–443.
[2] Scripps Keeling Curve Website: https://www.co2.earth, measured at Mauna Loa Observatory, Hawaii, 2018.
[3] National Centers for Environmental Information: https://www.ncei.noaa.gov, 2018.
[4] M.A.M. Kinnon, J. Brouwer, S. Samuelsen, The role of natural gas and its infrastructure in mitigating greenhouse gas emissions, improving regional air quality, and renewable resource integration, Prog. Energy Combust. Sci. 64 (2018) 62–92.
[5] M.Z. Jacobson, Review of solutions to global warming, air pollution, and energy security, Energy Environ. Sci. 2 (2009) 148–173.
[6] S.D. Kenarsari, D. Yang, G. Jiang, S. Zhang, J. Wang, A.G. Russell, Q. Wei, M. Fan, Review of recent advances in carbon dioxide separation and capture, RSC Adv. 3 (2013) 22739–22773.
[7] G. Göttlicher, R. Pruschek, Comparison of CO_2 removal systems for fossil-fuelled power plant processes, Energy Convers. Manag. 38 (1997) S173–S178.
[8] Y. Takamura, J. Aoki, S. Uchida, S. Narita, Application of high-pressure swing adsorption process for improvement of CO_2 recovery system from flue gas, Can. J. Chem. Eng. 79 (2001) 812–816.
[9] D. Aaron, C. Tsouris, Separation of CO_2 from Flue Gas: A Review, Sep. Sci. Technol. 402 (2005) 321–348.
[10] M.J. Tuinier, M. van Sint Annaland, G.J. Kramer, J.A.M. Kuipers, Cryogenic CO_2 capture using dynamically operated packed beds, Chem. Eng. Sci. 65 (2010) 114–119.
[11] A.S. Bhown, B.C. Freeman, Analysis and status of post-combustion carbon dioxide capture technologies, Environ. Sci. Technol. 45 (2011) 8624–8632.
[12] M. Clausse, J. Merel, F. Meunier, Numerical parametric study on CO_2 capture by indirect thermal swing adsorption, Int. J. Greenh. Gas Con. 5 (2011) 1206–1213.
[13] R. Dawson, A.I. Cooper, D. Adams, Chemical functionalization strategies for carbon dioxide capture in microporous organic polymers, Polym. Int. 62 (2013) 345–352.
[14] S. Sjostrom, H. Krutka, Evaluation of solid sorbents as a retrofit technology for CO_2 capture, Fuel 89 (2010) 1298–1306.
[15] R. Veneman, Z. Li, J. Hogendoorn, S. Kersten, D. Brilman, Continuous CO_2 capture in a circulating fluidized bed using supported amine sorbents, Chem. Eng. J. 207-208 (2012) 18–26.
[16] B. Lv, B. Guo, Z. Zhou, G. Jing, Mechanisms of CO_2 capture into monoethanolamine solution with different CO_2 loading during the absorption/desorption processes, Environ. Sci. Technol. 49 (2015) 10728–10735.
[17] S. Zulfiqar, D. Mantione, O. El Tall, M.I. Sarwar, F. Ruipérez, A. Rothenberger, D. Mecerreyes, Nanoporous amide networks based on tetraphenyladamantane for selective CO_2 capture, J. Mater. Chem. A 4 (2016) 8190–8197.
[18] E. González-Zamora, I.A. Ibarra, CO_2 capture under humid conditions in metal-organic frameworks, Mater. Chem. Front. 1 (2017) 1471–1484.
[19] J.C. Meyer, A.K. Geim, M.I. Katsnelson, K.S. Novoselov, T.J. Booth, S. Roth, The structure of suspended graphene sheets, Nature 446 (2007) 60–63.
[20] K. Scida, P.W. Stege, G. Haby, G.A. Messina, C.D. García, Recent applications of carbon-based nanomaterials in analytical chemistry: critical review, Anal. Chim. Acta 691 (2011) 6–17.
[21] J. Wang, F. Ma, W. Liang, M. Sun, Electrical properties and applications of graphene, hexagonal boron nitride (h-BN), and graphene/h-BN heterostructures, Mater. Today Phys. 2 (2017) 6–34.
[22] R.K. Matharu, H. Porwal, L. Ciric, M. Edirisinghe, The effect of graphene-poly (methyl methacrylate) fibres on microbial growth, Interface Focus 8 (2018) 20170058.
[23] M. Pykal, P. Jurečka, F. Karlický, M. Otyepka, Modelling of graphene functionalization, Phys. Chem. Chem. Phys. 18 (2016) 6351–6372.
[24] D. D'Alessandro, B. Smit, J. Long, Carbon dioxide capture: prospects for new materials, Angew. Chem. Int. Ed. 49 (2010) 6058–6082.
[25] S. Rodriguez-Couto, A. Arzac, G.P. Leal, R. Tomovska, Reduced graphene oxide hydrogels and xerogels provide efficient platforms for immobilization and laccase

production by *Trametes pubescens*, Biotechnol. J. 9 (2014) 578–584.
[26] Z. Yang, S. Chabi, Y. Xia, Y. Zhu, Preparation of 3D graphene-based architectures and their applications in supercapacitors, Pro. Nat. Sci-Mater. 25 (2015) 554–562.
[27] N. Ormategui, A. Veloso, G.P. Leal, S. Rodriguez-Couto, R. Tomovska, Design of stable and powerful nanobiocatalysts, based on enzyme laccase immobilized on self-assembled 3D graphene/polymer composite hydrogels, ACS Appl. Mater. Interfaces 7 (2015) 14104–14112.
[28] Z.-Y. Sui, B.-H. Han, Effect of surface chemistry and textural properties on carbon dioxide uptake in hydrothermally reduced graphene oxide, Carbon 82 (2015) 590–598.
[29] S. Chowdhury, R. Balasubramanian, Holey graphene frameworks for highly selective post-combustion carbon capture, Sci. Rep. 6 (2016) 21537.
[30] S. Gadipelli, Y. Lu, N.T. Skipper, T. Yildirim, Z. Guo, Design of hyperporous graphene networks and their application in solid-amine based carbon capture systems, J. Mater. Chem. A 5 (2017) 17833–17840.
[31] F.-Q. Liu, L.-L. Wang, G.-H. Li, W. Li, C.-Q. Li, Hierarchically structured graphene coupled microporous organic polymers for superior CO_2 capture, ACS Appl. Mater. Interfaces 9 (2017) 33997–34004.
[32] L. Ekhlasi, H. Younesi, A. Rashidi, N. Bahramifar, Populus wood biomass-derived graphene for high CO_2 capture at atmospheric pressure and estimated cost of production, Process Saf. Environ. 113 (2018) 97–108.
[33] J.A.A. Gibson, E. Mangano, E. Shiko, A.G. Greenaway, A.V. Gromov, M.M. Lozinska, D. Friedrich, E.E.B. Campbell, P.A. Wright, S. Brandani, Adsorption materials and processes for carbon capture from gas-fired power plants: AMPGas, Ind. Eng. Chem. Res. 55 (2016) 3840–3851.
[34] A.K. Mishra, S. Ramaprabhu, Carbon dioxide adsorption in graphene sheets, AIP Adv. 1 (2011) 032152.
[35] C.-S.T. Cheng-Hsiu Yu, Chih-Hung Huang, A review of CO_2 capture by absorption and adsorption, Aerosol Air Qual. Res. 12 (2012) 745–769.
[36] C. Liu, W. Xing, J. Zhou, S. ping Zhuo, N-containing activated carbons for CO_2 capture, Int. J. Smart Nano Mater. 4 (2013) 55–61.
[37] B. Wu, X. Yang, A molecular simulation of interactions between graphene nanosheets and supercritical CO_2, J. Colloid Interface Sci. 361 (2011) 1–8.
[38] Y. Liu, J. Wilcox, Molecular simulation studies of co_2 adsorption by carbon model compounds for carbon capture and sequestration applications, Environ. Sci. Technol. 47 (2012) 95–101.
[39] L. Joos, J.A. Swisher, B. Smit, Molecular simulation study of the competitive adsorption of H_2O and CO_2 in zeolite 13X, Langmuir 29 (2013) 15936–15942.
[40] Y. Liu, J. Wilcox, Molecular simulation studies of CO_2 adsorption by carbon model compounds for carbon capture and sequestration applications, Environ. Sci. Technol. 47 (2013) 95–101.
[41] S. Jiao, Z. Xu, Selective gas diffusion in graphene oxides membranes: a molecular dynamics simulations study, ACS Appl. Mater. Interfaces 7 (2015) 9052–9059.
[42] M. Rahimi, J.K. Singh, F. Müller-Plathe, Adsorption and separation of binary and ternary mixtures of SO_2, CO_2 and N_2 by ordered carbon nanotube arrays: grand-canonical Monte Carlo simulation, Phys. Chem. Chem. Phys. 18 (2016) 4112–4120.
[43] W. Li, X. Zheng, Z. Dong, C. Li, W. Wang, Y. Yan, J. Zhang, Molecular dynamics simulations of CO_2/N_2 separation through two-dimensional graphene oxide membranes, J. Phys. Chem. C 120 (2016) 26061–26066.
[44] T.T. Trinh, K.-Q. Tran, Q.-V. Bach, D.Q. Trinh, A Molecular dynamics simulation study on separation selectivity of CO_2/CH_4 mixture in mesoporous carbons, Energy Procedia 86 (2016) 144–149.
[45] V.S. Kandagal, F. Chen, E. Jónsson, J.M. Pringle, M. Forsyth, Molecular simulation study of CO_2 and N_2 absorption in a phosphonium based organic ionic plastic crystal, J. Chem. Phys. 147 (2017) 124703.
[46] M. Gao, A.J. Misquitta, C. Yang, I.T. Todorov, A. Mutter, M.T. Dove, Molecular dynamics study of CO_2 absorption and desorption in zinc imidazolate frameworks, Mol. Syst. Des. Eng. 2 (2017) 457–469.
[47] H. Wang, Z. Qu, J. Bai, Y. Qiu, Combined grand canonical Monte Carlo and finite volume method simulation method for investigation of direct air capture of low concentration CO_2 by 5A zeolite adsorbent bed, Int. J. Heat Mass Transf. 126 (2018) 1219–1235.
[48] A. Luzar, D. Chandler, Structure and hydrogen bond dynamics of water-dimethyl sulfoxide mixtures by computer simulations, J. Chem. Phys. 98 (1993) 8160–8173.
[49] B. Hess, C. Kutzner, D. van der Spoel, E. Lindahl, GROMACS 4: Algorithms for Highly Efficient, load-balanced, and scalable molecular simulation, J. Chem. Theory Comput. 4 (2008) 435–447.
[50] G. Bussi, D. Donadio, M. Parrinello, Canonical sampling through velocity rescaling, J. Chem. Phys. 126 (2007) 014101.
[51] J.J. Potoff, J.I. Siepmann, Vapor-liquid equilibria of mixtures containing alkanes, carbon dioxide, and nitrogen, AIChE J. 47 (2001) 1676–1682.
[52] J. Yang, Y. Ren, A.-m. Tian, H. Sun, COMPASS Force Field for 14 Inorganic Molecules, He, Ne, Ar, Kr, Xe, H_2, O_2, N_2, NO, CO, CO_2, NO_2, CS_2, and SO_2, in Liquid Phases, J. Phys. Chem. B 104 (2000) 4951–4957.
[53] J.G. Harris, K.H. Yung, Carbon dioxide's liquid-vapor coexistence curve and critical properties as predicted by a simple molecular model, J. Phys. Chem. 99 (1995) 12021–12024.
[54] C. Murthy, K. Singer, M. Klein, I. McDonald, Pairwise additive effective potentials for nitrogen, Mol. Phys. 41 (1980) 1387–1399.
[55] P.W. Atkins, J. de Paula, Physical Chemistry. 7th Edition. Oxford University Press, Oxford, UK, 2002.
[56] W.L. Jorgensen, D.S. Maxwell, J. Tirado-Rives, Development and testing of the OPLS all-atom force field on conformational energetics and properties of organic liquids, J. Am. Chem. Soc. 118 (1996) 11225–11236.
[57] R. Zangi, D. Roccatano, Strings-to-rings transition and antiparallel dipole alignment in two-dimensional methanols, Nano Lett. 16 (2016) 3142–3147.
[58] J.H. Walther, R. Jaffe, T. Halicioglu, P. Koumoutsakos, Carbon nanotubes in water: structural characteristics and energetics, J. Phys. Chem. B 105 (2001) 9980–9987.
[59] G.M. Meconi, N. Ballard, J.M. Asua, R. Zangi, Shedding light on the different behavior of ionic and nonionic surfactants in emulsion polymerization: from atomistic simulations to experimental observations, Phys. Chem. Chem. Phys. 19 (2017) 31692–31705.
[60] C. Tanford, Extension of the theory of linked functions to incorporate the effects of protein hydration, J. Mol. Biol. 39 (1969) 539–544.
[61] R. Zangi, R. Zhou, B.J. Berne, Urea's action on hydrophobic interactions, J. Am. Chem. Soc. 131 (2009) 1535–1541.
[62] J.H. Bae, Y.R. Lim, J. Sung, Statistical mechanics of molecular adsorption: effects of adsorbate interaction on isotherms, Langmuir 24 (2008) 2569–2572.
[63] C. Graham, J. Pierrus, R. Raab, Measurement of the electric quadrupole moments of CO_2, CO and N_2, Mol. Phys. 67 (1989) 939–955.
[64] X. Xu, C.D. Wood, A highly tunable approach to enhance CO_2 capture with liquid alkali/amines, Environ. Sci. Technol. 52 (2018) 10874–10882.

Supplementary Material:

Adsorption of CO_2 Gas on Graphene-Polymer Composites

Giulia Magi Meconi[1], Radmila Tomovska[1,3], and Ronen Zangi*[2,3]

[1] *POLYMAT & Department of Applied Chemistry, University of the Basque Country UPV/EHU, Avenida de Tolosa 72, 20018, San Sebastian, Spain*

[2] *POLYMAT & Department of Organic Chemistry I, University of the Basque Country UPV/EHU, Avenida de Tolosa 72, 20018, San Sebastian, Spain*

[3] *IKERBASQUE, Basque Foundation for Science, Maria Diaz de Haro 3, 48013 Bilbao, Spain*

March 8, 2019

*Corresponding author. Email: r.zangi@ikerbasque.org (Ronen Zangi)

Table S1: The density of CO_2 gas, in kg/m^3, in the bulk region of the simulation box for the different polymer-graphene composite systems as well as for bare graphene. $N°_{CO_2}$ is the total number of carbon dioxide molecules in the simulation box.

$N°_{CO_2}$	G	G-PMMA	G-PEAM	G-DAPM	G-PAAM	G-PDAFMA	G-PS
200	0.097	0.158	0.128	0.095	0.092	0.071	0.532
400	0.179	0.382	0.269	0.214	0.185	0.152	0.769
700	0.323	0.702	0.494	0.396	0.356	0.300	1.346
1400	0.722	1.945	1.120	1.009	0.937	0.792	2.352
2100	1.170	3.076	1.928	1.683	1.592	1.294	4.039
2700	1.663	3.926	2.789	2.470	2.399	1.875	5.194
3500	2.423	5.111	3.903	3.360	3.365	3.228	6.732
5250	4.547	8.199	6.526	6.186	5.578	5.065	9.171
7000	7.078	11.272	9.152	8.601	8.267	8.161	12.389

Table S2: The density of N_2 gas, in kg/m^3, in the bulk region of the simulation box for the different polymer-graphene composite systems as well as for bare graphene. $N°_{N_2}$ is the total number of nitrogen molecules in the simulation box.

$N°_{N_2}$	G	G-PMMA	G-PEAM	G-DAPM	G-PAAM	G-PDAFMA	G-PS
200	0.204	0.205	0.189	0.175	0.139	0.130	0.127
400	0.404	0.429	0.377	0.367	0.292	0.277	0.490
700	0.706	0.760	0.686	0.648	0.537	0.522	0.857
1400	1.416	1.599	1.425	1.359	1.157	0.744	1.754
2100	2.146	2.435	2.193	2.103	1.883	1.849	2.571
2700	2.796	3.139	2.876	2.798	2.492	2.465	3.305
3500	3.718	4.086	3.816	3.690	3.395	3.533	4.285
5250	5.801	6.216	5.814	5.655	5.216	5.164	6.616
7000	7.956	8.322	7.871	7.738	7.298	7.631	8.810

Table S3: The density of CH_4 gas, in kg/m^3, in the bulk region of the simulation box for the different polymer-graphene composite systems as well as for bare graphene. $N°_{CH_4}$ is the total number of methane molecules in the simulation box.

$N°_{CH_4}$	G	G-PMMA	G-PEAM	G-DAPM	G-PAAM	G-PDAFMA	G-PS
200	0.097	0.117	0.108	0.096	0.098	0.090	0.065
400	0.179	0.249	0.213	0.200	0.178	0.176	0.280
700	0.323	0.445	0.375	0.367	0.359	0.330	0.491
1400	0.722	0.993	0.812	0.815	0.792	0.744	0.982
2100	1.170	1.502	1.320	1.280	1.277	1.171	1.473
2700	1.420	1.923	1.771	1.733	1.741	1.555	1.893
3500	2.423	2.507	2.342	2.273	2.303	2.408	2.454
5250	4.547	3.816	3.669	3.646	3.582	3.489	3.846
7000	7.078	5.112	4.945	4.901	4.868	5.072	5.154

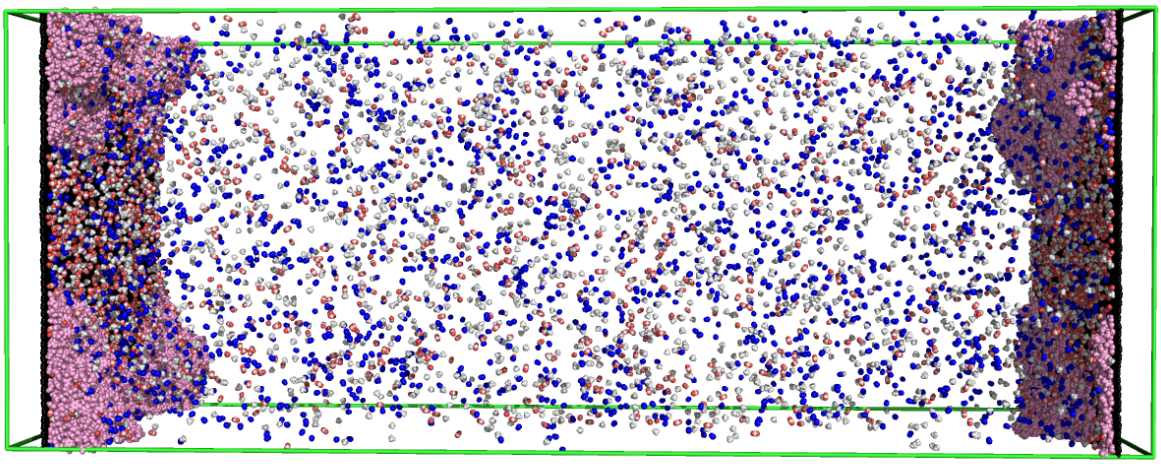

Figure S1: A snapshot of the last configuration of the G-PDAFMA composite system with $\frac{1}{3}N°_{gas}$=2700. Graphene is shown as black sticks, the polymer is colored in magenta with a sphere representation. Gas molecules are displayed as spheres, where hydrogens are colored in white, oxygens in red, nitrogens in blue and carbons in gray.

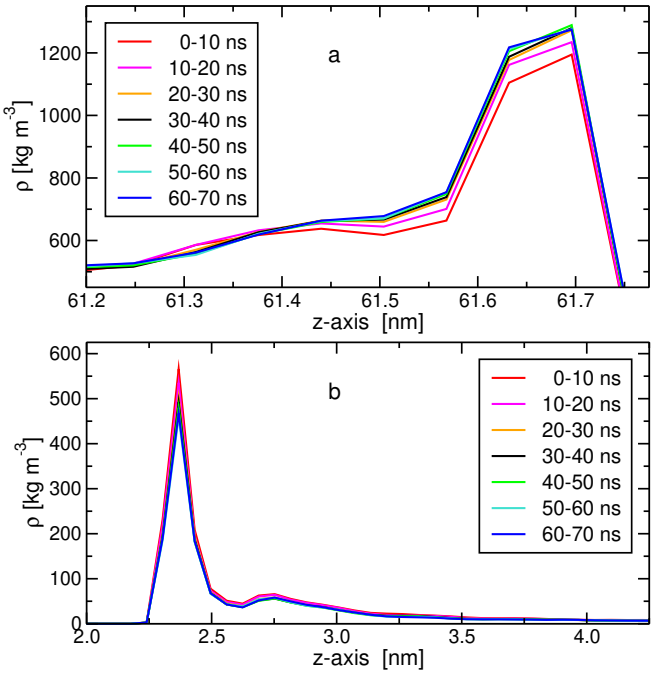

Figure S2: Convergence properties of the G-PAAM system with $N°_{gas}$=2700 as monitored by the density profile along the z-axis of (a) the polymer and (b) the CO_2 gas. The different curves are calculated for 10 ns consecutive segments of the 70 ns trajectory. Note that the CO_2 gas next to the other graphene sheet reached convergence even faster.

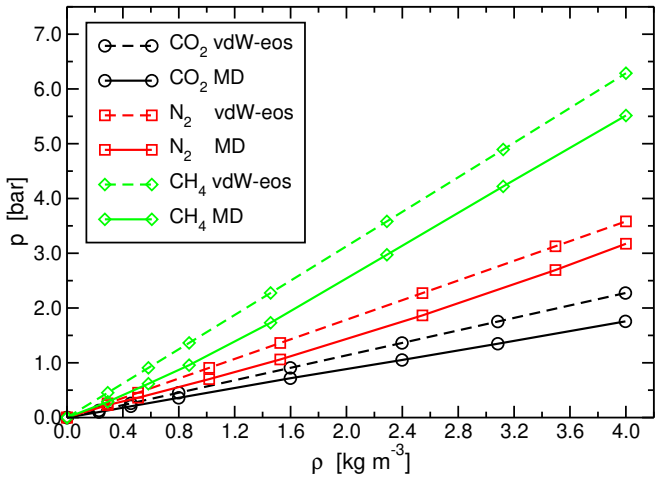

Figure S3: Pressure-density curves from simulations at 300 K of a homogeneous one-component bulk gas system for the CO_2, N_2, and CH_4 models employed in this study. The corresponding van der Waals equations of state, in which the a and b parameters were fitted to experimental results (see Table S4), are plotted for comparison. The NVT simulations were performed with a cubic box of 40.0 nm length for all densities. The random starting positions of the gas molecules were equilibrated for a time period of 30 ns with an additional 10 ns of data collection step. Other simulation details were the same as those described for the graphene-polymer composite systems.

Table S4: The experimentally determined coefficients[1] of the van der Waals equation of state, $p = nRT/(V - nb) - an^2/V^2$, for CO_2, N_2, CH_4. In this equation, p, V, T, n, and R, are the pressure, volume, temperature, number of moles, and the gas constant, respectively.

	a [atm·L^2·mol^{-2}]	b [10^{-2}·L·mol^{-1}]
CO_2	3.610	4.290
N_2	1.352	3.870
CH_4	2.273	4.310

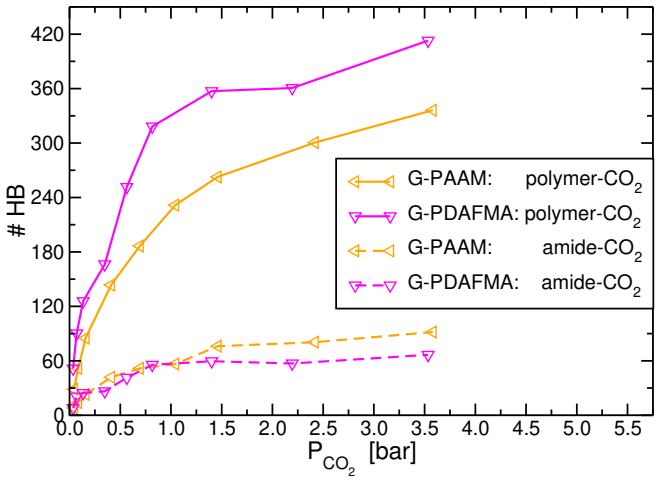

Figure S4: The contribution of the amide group in PAAM and PDAFMA (the group connecting the backbone to the aromatic rings) to the formation of hydrogen bonds between the polymer and CO_2. Solid-lines exhibit the total number of hydrogen bonds between the polymer and CO_2 (same as those shown in Fig. 9) whereas the dashed-lines the values only due the amide groups.

Force-Felds of the Polymers Considered in this Study

The different polymers were modeled based on the OPLSAA force-field. In this force field, the different energetic terms of the potential energy function assume the following functional forms,

$$\textit{Bond stretching:} \qquad \mathrm{E_{bond}} = \sum_{\mathrm{bonds}} \mathrm{K_b}(\mathrm{r} - \mathrm{r_0})^2$$

$$\textit{Angle bending:} \qquad \mathrm{E_{angle}} = \sum_{\mathrm{angles}} \mathrm{K}_\theta(\theta - \theta_0)^2$$

Dihedral angle torsion (Ryckaert-Bellemans):

$$\mathrm{E_{torsion}}(\phi_{\mathrm{ijkl}}) = \sum_{\mathrm{torsions}} \frac{1}{2}[\mathrm{C_1}(1 + \cos(\phi)) + \mathrm{C_2}(1 - \cos(2\phi)) + \mathrm{C_3}(1 + \cos(3\phi)) + \mathrm{C_4}(1 - \cos(4\phi))]$$

$$\textit{Improper dihedral angle:} \qquad \mathrm{E_{improper}}(\phi_{\mathrm{ijkl}}) = \mathrm{k}_\phi(1 + \cos(\mathrm{n}\phi - \phi_{\mathrm{s}}))$$

Non-bonded interactions:

$$\mathrm{E_{non-bonded}} = \sum_{\mathrm{i}} \sum_{\mathrm{j>i}} \left\{ 4\epsilon_{\mathrm{ij}} \left[\left(\frac{\sigma_{\mathrm{ij}}}{\mathrm{r_{ij}}} \right)^{12} - \left(\frac{\sigma_{\mathrm{ij}}}{\mathrm{r_{ij}}} \right)^{6} \right] + \frac{\mathrm{q_i q_j e^2}}{\mathrm{r_{ij}}} \right\}$$

$$\textit{combination rule:} \qquad \sigma_{\mathrm{ij}} = \frac{\sigma_{\mathrm{ii}} + \sigma_{\mathrm{jj}}}{2} \qquad , \qquad \epsilon_{\mathrm{ij}} = \sqrt{\epsilon_{\mathrm{ii}} \epsilon_{\mathrm{jj}}}$$

A Model for Poly(styrene)

The stereochemistry of each unit in the PS chain is randomly generated during polymerization. Therefore, we chose to model each chain with alternating C_α chiral centers (R followed by S). The bonded and non-bonded parameters of PS were taken from the OPLS-AA model of ethylbenzene[2, 3]. However, in order to allow the connectivity between the subunits and simultaneously maintain zero charge for each of these subunits, we made the following changes. The partial charge of C_β of the first residue was changed from -0.180 to -0.120, that of C_γ of the last residue was changed from -0.115 to -0.055, and both changes were applied to the repeating residues. The resulting model is shown in Fig. S5 and the non-bonded interactions are specified in Table S5. Using this model, we obtained a value of 1.02 kg/m^3 for the density of amorphous PS which is close to its experimental value[4] of 1.04–1.06 kg/m^3. Furthermore, the calculated values of the radius of gyration, 9.8 Å, and the weight-normalized end-to-end distance squared, 0.42 Å$^2\cdot$ mol/g, are also in a very good agreement with their experimentally determined values of 10.0 Å and 0.43 Å$^2\cdot$ mol/g, respectively, as well as with other models for PS[5, 6, 7].

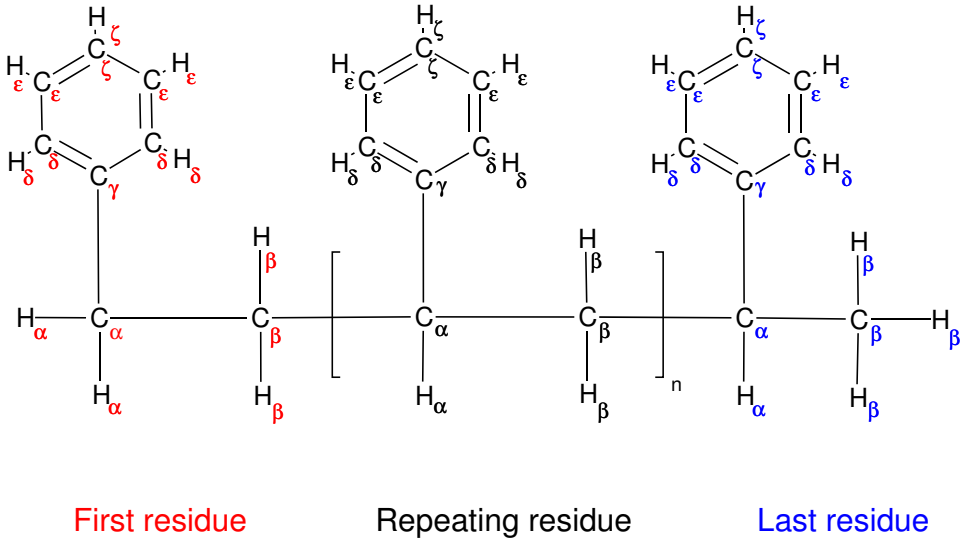

Figure S5: The model for poly(styrene) based on the OPLS-AA force-field. The partial charge and LJ parameters describing each atom is detailed in Table S5. Note that the C_α of the repeating and last residues are chirals, nevertheless, the parameters for the R and S configurations are the same.

Table S5: Partial charges and LJ parameters for the poly(styrene) model. The values refer to all residue types (first, repeating, and last) unless otherwise indicated.

	q [e]	σ [nm]	ϵ [kJ/mol]
C_α	-0.005	0.350	0.276
C_β	-0.120	0.350	0.276
$C_{\beta,\text{last}}$	-0.180	0.350	0.276
C_γ	-0.055	0.355	0.293
$C_{\gamma,\text{first}}$	-0.115	0.355	0.293
H_α, H_β	+0.060	0.250	0.126
C_δ, C_ϵ, C_ζ	-0.115	0.355	0.293
H_δ, H_ϵ, H_ζ	+0.115	0.242	0.126

A Model for poly(methyl methacrylate) (PMMA)

The partial charges and bonded parameters for PMMA were adopted from the model proposed by Maranas[8]. To allow the connectivity between the subunits and simultaneously maintain zero charge for each of these subunits, we made the following change. The partial charge of C_α of the first and last residue was changed from 0.00 to -0.045. No variations were applied to the partial charges of the repeating residues. The resulting model is displayed in Figure S6 and the non-bonded interactions are specified in Table S6. The LJ parameters were taken from the OPLS-AA force field. Bond, angle and dihedral parameters, proposed by Maranas [8] are employed in this study and are shown in Table S7, S8 and S9, respectively.

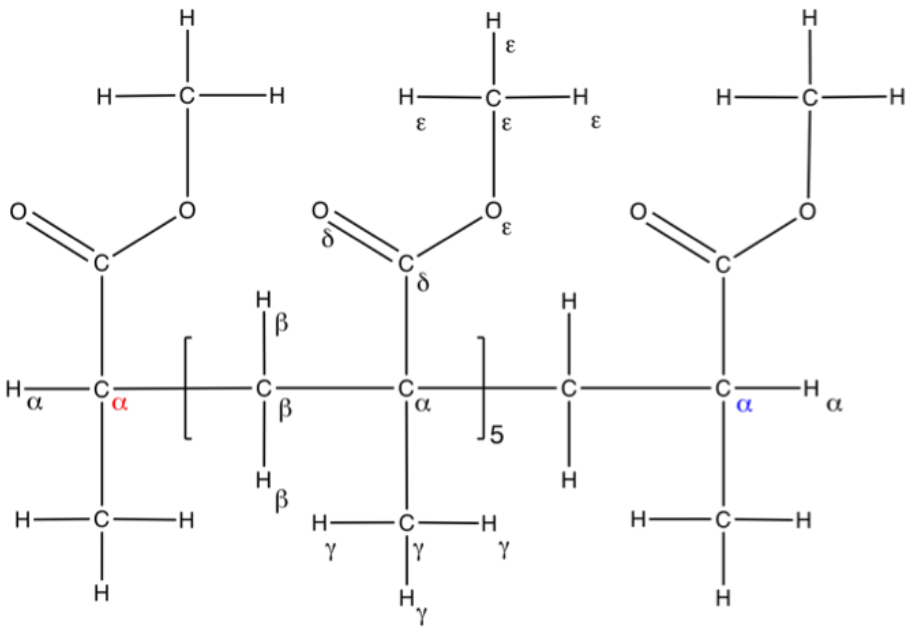

Figure S6: The chemical structure of PMMA polymer with the different atom types.

Atom Type	q [e]	σ [nm]	ε [kJ mol^{-1}]
Cγ	-0.135	0.350	0.276
Cα, Cα, terminal	-0.045	0.350	0.276
Cα	0.000	0.350	0.276
Cβ	-0.090	0.350	0.276
Cδ	0.510	0.375	0.439
Oδ	-0.430	0.296	0.879
Oε	-0.330	0.300	0.711
Cε	0.160	0.350	0.276
Hγ, Hα, Hβ	0.045	0.250	0.126
Hε	0.030	0.250	0.126

Table S6: Partial charges and LJ parameters for PMMA model.

Bond Type	r_o [nm]	K_{bond} [kJ mol^{-1}nm^{-2}]
Cγ-Hγ	0.10900	138490.4
Cγ-Cα	0.15390	153971.2
Cα-Hα	0.10900	138490.4
Cα-Cβ	0.15491	125520.0
Cβ-Hβ	0.10900	138490.4
Cα-Cδ	0.15710	136398.4
Cδ-Oδ	0.12290	405011.2
Cδ-Oε	0.13600	197066.4
Cε-Oε	0.14460	143092.8
Cε-Hε	0.10900	138490.4

Table S7: Bond vibration parameters of PMMA polymer.

Angle Type	θ_0 [deg]	K_{angle} [kJ mol^{-1} rad^{-2}]
Hγ-Cγ-Hγ	109.50	146.4400
Hγ-Cγ-Cα	109.50	146.4400
Cγ-Cα-Cβ	109.47	367.7736
Cγ-Cα-Cδ	109.47	367.7736
Cα-Cδ-Oδ	125.60	264.8472
Cα-Cδ-Oε	111.40	311.7080
Hβ-Cβ-Cα	109.50	146.4400
Hβ-Cβ-Hβ	109.50	146.4400
Oδ-Cδ-Oε	123.00	529.2760
Cδ-Oε-Cε	116.40	354.8032
Hε-Cε-Oε	110.10	243.3040
Hε-Cε-Hε	109.50	146.4400
Cα-Cβ-Cα	113.30	374.4680

Table S8: Angle bending parameters of PMMA.

Dihedral Type	C_0 [kJ mol^{-1}]	C_1 [kJ mol^{-1}]	C_2 [kJ mol^{-1}]	C_3 [kJ mol^{-1}]	C_4 [kJ mol^{-1}]	C_5 [kJ mol^{-1}]
Cγ-Cα-Cδ-Oδ	0.31380	-21.4430	-0.20920	21.3384	0.00000	0.00000
Cβ-Cα-Cδ-Oδ	0.31380	-21.4430	-0.20920	21.3384	0.00000	0.00000
Cγ-Cα-Cδ-Oε	1.69000	-1.69000	-13.52001	0.00000	13.52001	0.00000
Cβ-Cα-Cδ-Oε	1.69000	-1.69000	-13.52001	0.00000	13.52001	0.00000
Cε-Oε-Cδ-Cα	1.50624	0.16736	-1.17152	-5.85760	5.35552	0.00000
Cγ-Cα-Cβ-Cα	0.58141	-0.58141	-4.65127	0.00000	4.65127	0.00000
Cδ-Cα-Cβ-Cα	0.58141	-0.58141	-4.65127	0.00000	4.65127	0.00000

Table S9: Ryckaert-Bellemans dihedral angle parameters of PMMA.

A Model for poly(2-aminoethyl methacrylate) (PEAM)

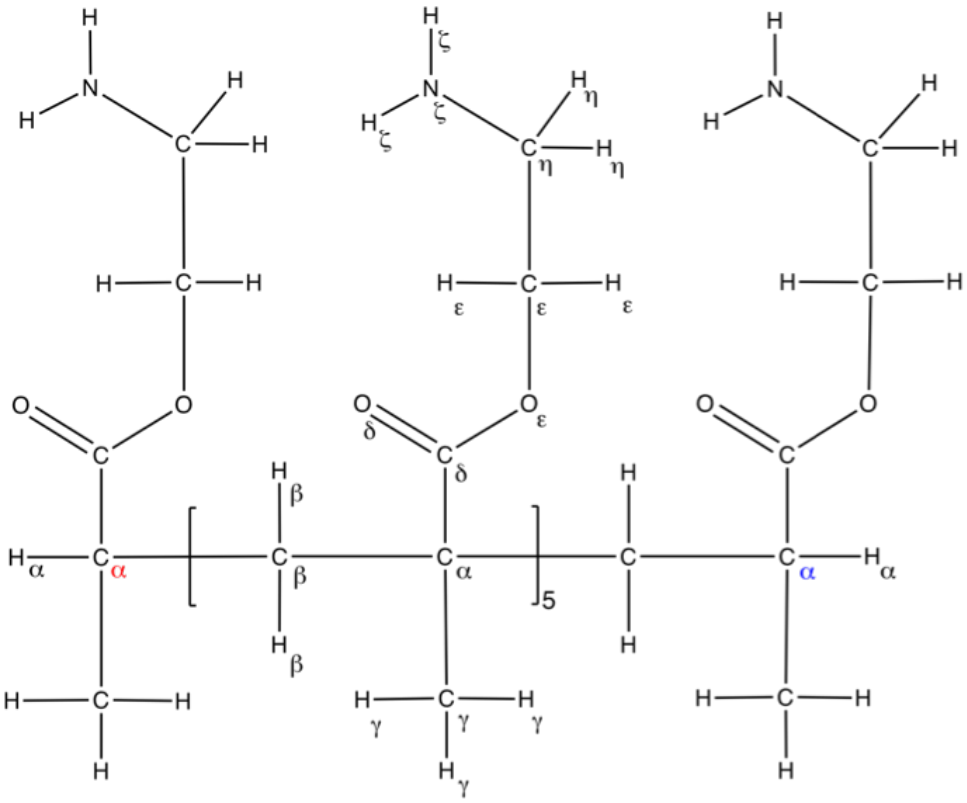

Figure S7: The partial charges and bonded parameters for the atoms which are part of the methylene methacrylate group are taken from the PMMA model of Maranas[8]. These interaction terms are detailed in Table S10, S11, S12 and S13. Bonded interactions needed for an all-atom description were then adopted from the corresponding interactions of the OPLS-AA force field.

Atom Type	q [e]	σ [nm]	ε [kJ mol^{-1}]
Cγ	-0.135	0.350	0.276
Cα, Cα, terminal	-0.045	0.350	0.276
Cα	0.000	0.350	0.276
Cβ	-0.090	0.350	0.276
Cδ	0.510	0.375	0.439
Oδ	-0.430	0.296	0.879
Oε	-0.330	0.300	0.711
Cε	0.190	0.350	0.276
Cη	0.060	0.350	0.276
Nζ	-0.900	0.330	0.711
Hγ, Hα, Hβ	0.045	0.250	0.126
Hε	0.030	0.250	0.126
Hη	0.060	0.250	0.628
Hζ	0.360	0.000	0.000

Table S10: Partial charges and LJ parameters for PEAM. To maintain zero charge in each subunit, the partial charge of C_ϵ was changed from 0.160 to 0.190, and that of C_α of the first and last residue was changed from 0.00 to -0.045.

Bond Type	r_0 [nm]	K_{bond} [kJ mol^{-1}nm^{-2}]
Cγ-Hγ	0.10900	138490.4
Cγ-Cα	0.15390	153971.2
Cα-Hα	0.10900	138490.4
Cα-Cβ	0.15491	125520.0
Cβ-Hβ	0.10900	138490.4
Cα-Cδ	0.15710	136398.4
Cδ-Oδ	0.12290	405011.2
Cδ-Oε	0.13600	197066.4
Cε-Oε	0.14460	143092.8
Cε-Hε	0.10900	138490.4

Table S11: Bond vibration parameters of PEAM polymer.

Angle Type	θ_0 [deg]	K_{angle} [kJ mol^{-1} rad^{-2}]
Hγ-Cγ-Hγ	109.50	146.4400
Hγ-Cγ-Cα	109.50	146.4400
Cγ-Cα-Cβ	109.47	367.7736
Cγ-Cα-Cδ	109.47	367.7736
Cα-Cδ-Oδ	125.60	264.8472
Cα-Cδ-Oε	111.40	311.7080
Hβ-Cβ-Cα	109.50	146.4400
Hβ-Cβ-Hβ	109.50	146.4400
Oδ-Cδ-Oε	123.00	529.2760
Cδ-Oε-Cε	116.40	354.8032
Hε-Cε-Oε	110.10	243.3040
Hε-Cε-Hε	109.50	146.4400
Cα-Cβ-Cα	113.30	374.4680

Table S12: Angle bending parameters of PEAM.

Dihedral Type	C_0 [kJ mol^{-1}]	C_1 [kJ mol^{-1}]	C_2 [kJ mol^{-1}]	C_3 [kJ mol^{-1}]	C_4 [kJ mol^{-1}]	C_5 [kJ mol^{-1}]
Cγ-Cα-Cδ-Oδ	0.31380	-21.4430	-0.20920	21.3384	0.00000	0.00000
Cβ-Cα-Cδ-Oδ	0.31380	-21.4430	-0.20920	21.3384	0.00000	0.00000
Cγ-Cα-Cδ-Oε	1.69000	-1.69000	-13.52001	0.00000	13.52001	0.00000
Cβ-Cα-Cδ-Oε	1.69000	-1.69000	-13.52001	0.00000	13.52001	0.00000
Cε-Oε-Cδ-Cα	1.50624	0.16736	-1.17152	-5.85760	5.35552	0.00000
Cγ-Cα-Cβ-Cα	0.58141	-0.58141	-4.65127	0.00000	4.65127	0.00000
Cδ-Cα-Cβ-Cα	0.58141	-0.58141	-4.65127	0.00000	4.65127	0.00000
Nλ-Cη-Cε-Oε	16.73600	-16.73600	0.00000	0.00000	0.00000	0.00000

Table S13: Dihedral angles of PEAM polymer.

A Model for poly(3-diamin-(aminomethyl)propyl methacrylate) (DAPM)

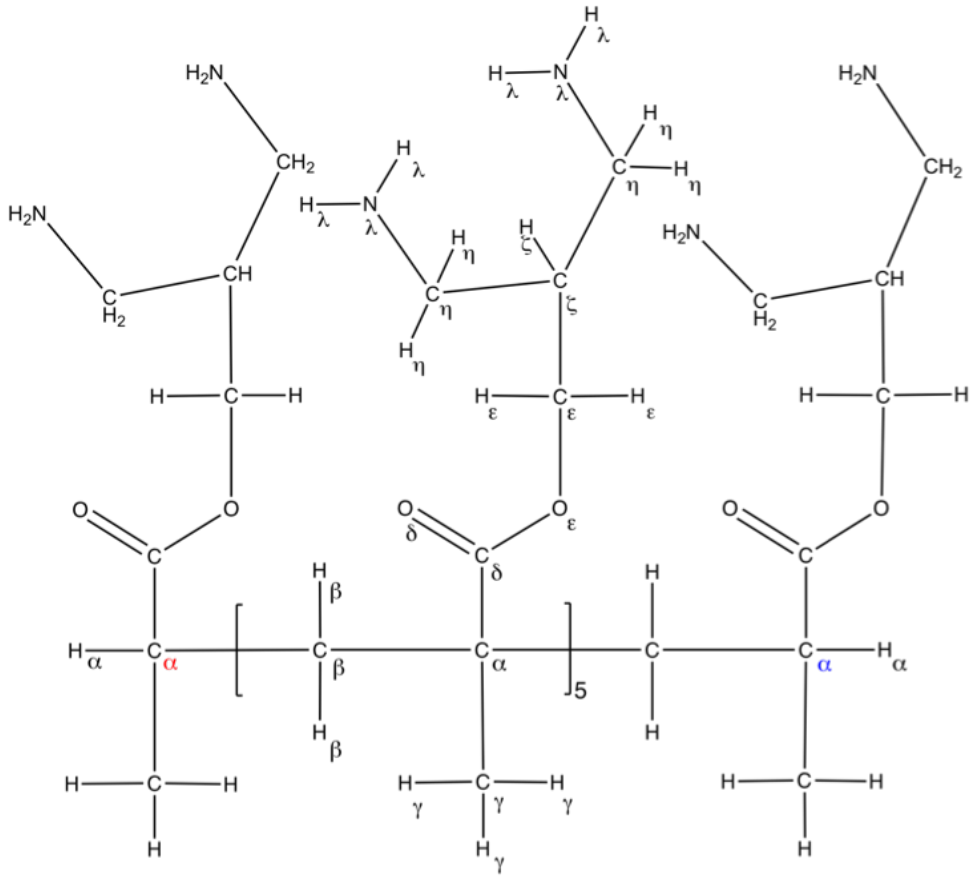

Figure S8: The partial charges and bonded parameters for the atoms of the methylene methacrylate group are taken from the model of Maranas[8]. These parameters are shown in Table S14, S15, S16 and S17. Bonded interactions not present for all-atom description were taken from the corresponding interactions of the OPLS-AA force field.

Atom Type	q [e]	σ [nm]	ε [kJ mol^{-1}]
Cγ	-0.135	0.350	0.276
Cα, Cα, terminal	-0.045	0.350	0.276
Cα	0.000	0.350	0.276
Cβ	-0.090	0.350	0.276
Cδ	0.510	0.375	0.439
Oδ	-0.430	0.296	0.879
Oε	-0.330	0.300	0.711
Cε	0.190	0.350	0.276
Cζ	-0.060	0.350	0.276
Cη	0.060	0.350	0.276
Nλ	-0.900	0.330	0.711
Hγ, Hα, Hβ	0.045	0.250	0.126
Hε	0.030	0.250	0.126
Hζ	0.060	0.250	0.126
Hη	0.060	0.250	0.063
Hλ	0.360	0.000	0.000

Table S14: Partial charges and LJ parameters for DAPM. To maintain zero charge in each subunit, the partial charge of C_ε was changed from 0.160 to 0.190, and that of C_α of the first and last residue was changed from 0.00 to -0.045. Nonbonded parameters are taken from OPLS-AA force field.

Bond Type	r_0 [nm]	K_{bond} [kJ $mol^{-1}nm^{-2}$]
Cγ-Hγ	0.10900	138490.4
Cγ-Cα	0.15390	153971.2
Cα-Hα	0.10900	138490.4
Cα-Cβ	0.15491	125520.0
Cβ-Hβ	0.10900	138490.4
Cα-Cδ	0.15710	136398.4
Cδ-Oδ	0.12290	405011.2
Cδ-Oε	0.13600	197066.4
Cε-Oε	0.14460	143092.8
Cε-Hε	0.10900	138490.4

Table S15: Bond vibration parameters of DAPM polymer.

Angle Type	θ_0 [deg]	K_{angle} [kJ mol^{-1} rad^{-2}]
Hγ-Cγ-Hγ	109.50	146.4400
Hγ-Cγ-Cα	109.50	146.4400
Cγ-Cα-Cβ	109.47	367.7736
Cγ-Cα-Cδ	109.47	367.7736
Cα-Cδ-Oδ	125.60	264.8472
Cα-Cδ-Oε	111.40	311.7080
Hβ-Cβ-Cα	109.50	146.4400
Hβ-Cβ-Hβ	109.50	146.4400
Oδ-Cδ-Oε	123.00	529.2760
Cδ-Oε-Cε	116.40	354.8032
Hε-Cε-Oε	110.10	243.3040
Hε-Cε-Hε	109.50	146.4400
Cα-Cβ-Cα	113.30	374.4680

Table S16: Angle bending parameters of DAPM polymer.

Dihedral Type	**C_0** [kJ mol^{-1}]	**C_1** [kJ mol^{-1}]	**C_2** [kJ mol^{-1}]	**C_3** [kJ mol^{-1}]	**C_4** [kJ mol^{-1}]	**C_5** [kJ mol^{-1}]
Cγ-Cα-Cδ-Oδ	0.31380	-21.4430	-0.20920	21.3384	0.00000	0.00000
Cβ-Cα-Cδ-Oδ	0.31380	-21.4430	-0.20920	21.3384	0.00000	0.00000
Cγ-Cα-Cδ-Oε	1.69000	-1.69000	-13.52001	0.00000	13.52001	0.00000
Cβ-Cα-Cδ-Oε	1.69000	-1.69000	-13.52001	0.00000	13.52001	0.00000
Cε-Oε-Cδ-Cα	1.50624	0.16736	-1.17152	-5.85760	5.35552	0.00000
Cγ-Cα-Cβ-Cα	0.58141	-0.58141	-4.65127	0.00000	4.65127	0.00000
Cδ-Cα-Cβ-Cα	0.58141	-0.58141	-4.65127	0.00000	4.65127	0.00000

Table S17: Dihedral angle parameters of DAPM polymer.

A Model for poly(aniline methacrylamide) (PAAM)

The partial charges and bonded parameters for C_γ, C_α, C_β, and H_γ, H_α, H_β were adopted from the model proposed for PMMA [8] polymer, as well as for the bonded parameters for C_δ-O_δ atom types. The LJ parameters were taken from the OPLS-AA force field. Dihedral parameters for C_δ-N_ϵ-C_ζ-C_η, C_η-C_ζ-N_ϵ-H_ϵ, C_λ-C_μ-N_υ-H_υ angles are taken from the parametrization of Rizzo and Jorgensen[9]. The Improper dihedrals terms derived from OPLS-AA force field. The sum of the charges for each subunit is zero; therefore, the partial charge of C_α of the first and last residue was changed from 0.00 to -0.045. Bonded interactions that were not detailed for all-atom description were taken from the corresponding interactions of the OPLS-AA force field. The resulting model is displayed in Figure S9. The partial charge and nonbonded parameters are shown in Table S18. Bond, angle, dihedral and improper dihedral parameters, are detailed in the Table S19, S20, S21, S22, respectively.

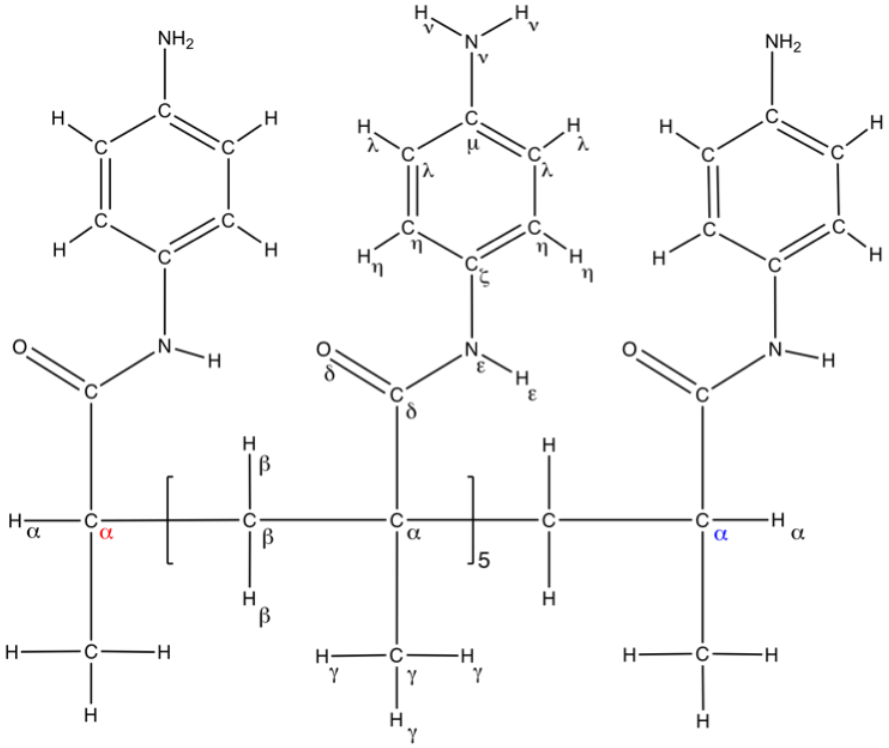

Figure S9: The chemical structure of PAAM polymer with the different atom types.

Atom Type	q [e]	σ [nm]	ε [kJ mol^{-1}]
Cγ	-0.135	0.350	0.276
Cα, Cα, terminal	-0.045	0.350	0.276
Cα	0.000	0.350	0.276
Cβ	-0.090	0.350	0.276
Cδ	0.500	0.375	0.439
Oδ	-0.500	0.296	0.879
Nε	-0.500	0.325	0.711
Cζ	0.200	0.355	0.293
Cη	-0.115	0.355	0.293
Cλ	-0.115	0.355	0.293
Cμ	0.180	0.355	0.293
Nv	-0.900	0.330	0.711
Hγ, Hα, Hβ	0.045	0.250	0.126
Hε	0.300	0.000	0.000
Hη, Hλ	0.115	0.355	0.293
Hv	0.360	0.000	0.000

Table S18: Partial charges and LJ parameters of PAAM polymer.

Bond Type	r_0 [nm]	K_{bond} [kJ mol^{-1}nm^{-2}]
Cγ-Hγ	0.10900	138490.4
Cγ-Cα	0.15390	153971.2
Cα-Hα	0.10900	138490.4
Cα-Cβ	0.15491	125520.0
Cβ-Hβ	0.10900	138490.4
Cα-Cδ	0.15710	136398.4
Cδ-Oδ	0.12290	405011.2

Table S19: Bond vibration parameters of PAAM polymer.

Angle Type	θ_0 [deg]	K_{angle} [kJ mol^{-1} rad^{-2}]
Hγ-Cγ-Hγ	109.50	146.4400
Hγ-Cγ-Cα	109.50	146.4400
Cγ-Cα-Cβ	109.47	367.7736
Cγ-Cα-Cδ	109.47	367.7736
Cα-Cδ-Oδ	125.60	264.8472
Hβ-Cβ-Cα	109.50	146.4400
Hβ-Cβ-Hβ	109.50	146.4400
Cα-Cβ-Cα	113.30	374.4680

Table S20: Angle bending parameters of PAAM polymer.

Dihedral Type	C_0 [kJ mol^{-1}]	C_1 [kJ mol^{-1}]	C_2 [kJ mol^{-1}]	C_3 [kJ mol^{-1}]	C_4 [kJ mol^{-1}]	C_5 [kJ mol^{-1}]
Cγ-Cα-Cδ-Oδ	0.31380	-21.4430	-0.20920	21.3384	0.00000	0.00000
Cβ-Cα-Cδ-Oδ	0.31380	-21.4430	-0.20920	21.3384	0.00000	0.00000
Cγ-Cα-Cβ-Cα	0.58141	-0.58141	-4.65127	0.00000	4.65127	0.00000
Cδ-Cα-Cβ-Cα	0.58141	-0.58141	-4.65127	0.00000	4.65127	0.00000
Cδ-Nε-Cζ-Cη	1.23900	8.58800	-3.43100	-6.39600	0.00000	0.00000
Cη-Cζ-Nε-Hε	2.03000	0.00000	-2.03000	0.00000	0.00000	0.00000
Cλ-Cμ-Nν-Hν	2.03000	0.00000	-2.03000	0.00000	0.00000	0.00000

Table S21: Dihedral angle parameters of PAAM polymer.

Improper Type	ϕ_s [deg]	K_ϕ [kJ mol^{-1}]
Cη-Cζ-Cη-Nε	180.0	4.60240
Cζ-Cη-Cλ-Hη	180.0	4.60240
Cη-Cλ-Cμ-Nλ	180.0	4.60240
Cλ-Cμ-Cλ-Hμ	180.0	4.60240
Cμ-Cλ-Cη-Nλ	180.0	4.60240
Cλ-Cη-Cζ-Hη	180.0	4.60240

Table S22: Improper dihedral angle parameters of PAAM polymer.

A Model for poly(N-(3,5-diaminophenyl)methacrylamide) (PDAFMA)

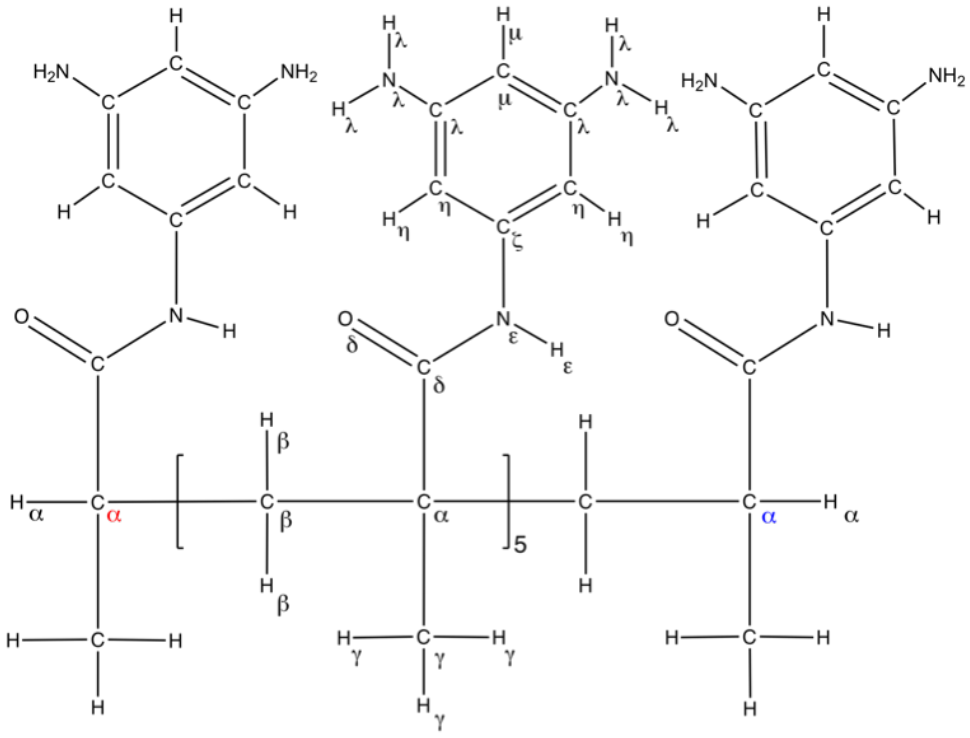

Figure S10: The chemical structure of PDAFMA polymer with the different atom types.

Atom Type	q [e]	σ [nm]	ε [kJ mol^{-1}]
Cγ	-0.135	0.350	0.276
Cα, Cα, terminal	-0.045	0.350	0.276
Cα	0.000	0.350	0.276
Cβ	-0.090	0.350	0.276
Cδ	0.500	0.375	0.439
Oδ	-0.500	0.296	0.879
Nε	-0.500	0.325	0.711
Cζ	0.200	0.355	0.293
Cη	-0.115	0.355	0.293
Cλ	0.180	0.355	0.293
Nλ	-0.900	0.330	0.711
Cμ	-0.115	0.355	0.293
Hγ, Hα, Hβ	0.045	0.250	0.126
Hε	0.300	0.000	0.000
Hη, Hμ	0.115	0.242	0.126
Hλ	0.360	0.000	0.000

Table S23: Partial charges and LJ parameters of PDAFMA polymer. The partial charges and bonded parameters for C_γ, C_α, C_β, and H_γ, H_α, C_β were adopted from the model proposed by Maranas[8]. This model was also used to define the bonded parameters for C_δ and O_δ atoms. To maintain zero charges for each subunit, the partial charge of C_α of the first and last residue was changed from 0.00 to -0.045. The LJ parameters were taken from the OPLS-AA force field.

Bonded interactions needed for the all-atom description but were not specified in the Maranas model[8] were taken from the corresponding interactions of the OPLS-AA force field.

Bond Type	r_0 [nm]	K_{bond} [kJ $mol^{-1}nm^{-2}$]
Cγ-Hγ	0.10900	138490.4
Cγ-Cα	0.15390	153971.2
Cα-Hα	0.10900	138490.4
Cα-Cβ	0.15491	125520.0
Cβ-Hβ	0.10900	138490.4
Cα-Cδ	0.15710	136398.4
Cδ-Oδ	0.12290	405011.2

Table S24: Bond vibration parameters of PDAFMA polymer.

Angle Type	θ_0 [deg]	K_{angle} [kJ mol^{-1} rad^{-2}]
Hγ-Cγ-Hγ	109.50	146.4400
Hγ-Cγ-Cα	109.50	146.4400
Cγ-Cα-Cβ	109.47	367.7736
Cγ-Cα-Cδ	109.47	367.7736
Cα-Cδ-Oδ	125.60	264.8472
Hβ-Cβ-Cα	109.50	146.4400
Hβ-Cβ-Hβ	109.50	146.4400
Cα-Cβ-Cα	113.30	374.4680

Table S25: Angle bending parameters of PDAFMA polymer.

Dihedral Type	C_0 [kJ mol^{-1}]	C_1 [kJ mol^{-1}]	C_2 [kJ mol^{-1}]	C_3 [kJ mol^{-1}]	C_4 [kJ mol^{-1}]	C_5 [kJ mol^{-1}]
Cγ-Cα-Cδ-Oδ	0.31380	-21.4430	-0.20920	21.3384	0.00000	0.00000
Cβ-Cα-Cδ-Oδ	0.31380	-21.4430	-0.20920	21.3384	0.00000	0.00000
Cγ-Cα-Cβ-Cα	0.58141	-0.58141	-4.65127	0.00000	4.65127	0.00000
Cδ-Cα-Cβ-Cα	0.58141	-0.58141	-4.65127	0.00000	4.65127	0.00000
Cδ-Nε-Cζ-Cη	1.23900	8.58800	-3.43100	-6.39600	0.00000	0.00000
Cη-Cζ-Nε-Hε	2.03000	0.00000	-2.03000	0.00000	0.00000	0.00000
Cμ-Cλ-Nλ-Hλ	2.03000	0.00000	-2.03000	0.00000	0.00000	0.00000
Cη-Cλ-Nλ-Hλ	2.03000	0.00000	-2.03000	0.00000	0.00000	0.00000

Table S26: Dihedral angle parameters of PDAFMA polymer. The parameters for C_δ-N_ϵ-C_ζ-C_η, C_η-C_ζ-N_ϵ-H_ϵ, C_μ-C_λ-N_λ-H_λ and C_μ-C_λ-N_λ-H_λ angle, are taken from Jorgensen et al.[9] parametrization.

Improper Type	ϕ_s [deg]	K_ϕ [kJ mol^{-1}]
Cη-Cζ-Cη-Nε	180.0	4.60240
Cζ-Cη-Cλ-Hη	180.0	4.60240
Cη-Cλ-Cμ-Hλ	180.0	4.60240
Cλ-Cμ-Cλ-Nv	180.0	4.60240
Cμ-Cλ-Cη-Hλ	180.0	4.60240

Table S27: Improper dihedral angle parameters of PDAFMA polymer. The terms derive from OPLS-AA force field.

References

[1] P. W. Atkins, J. de Paula, Physical Chemistry, seventh edition Edition, Oxford University Press, Oxford, UK, 2002.

[2] W. L. Jorgensen, D. L. Severance, Aromatic-Aromatic Interactions: Free Energy Profiles for the Benzene Dimer in Water, Chloroform and Liquid Benzene, J. Am. Chem. Soc. 112 (1990) 4768–4774.

[3] M. L. P. Price, D. Ostrovsky, W. L. Jorgensen, Gas-Phase and Liquid-State Properties of Esters, Nitriles, and Nitro Compounds with the OPLS-AA Force Field, J. Comp. Chem. 22 (2001) 1340–1352.

[4] J. Brandrup, E. H. Immergut, E. A. Grulke, Polymer Handbook, 4th Edition, Wiley, New York, 2003.

[5] L. J. Fetters, D. J. Lohse, D. Richter, T. A. Witten, A. Zirkel, Connection between Polymer Molecular Weight, Density, Chain Dimensions, and Melt Viscoelastic Properties, Macromolecules 27 (1994) 4639–4647.

[6] V. A. Harmandaris, N. P. Adhikari, N. F. A. van der Vegt, K. Kremer, Hierarchical Modeling of Polystyrene: From Atomistic to Coarse-Grained Simulations, Macromolecules 39 (2006) 6708–6719.

[7] T. Spyriouni, C. Tzoumanekas, D. Theodorou, F. Müller-Plathe, G. Milano, Coarse-Grained and Reverse-Mapped United-Atom Simulations of Long-Chain Atactic Polystyrene Melts: Structure, Thermodynamic Properties, Chain Conformation, and Entanglements, Macromolecules 40 (2007) 3876–3885.

[8] C. Chen, J. K. Maranas, V. García-Sakai, Local Dynamics of Syndiotactic Poly(methyl methacrylate) Using Molecular Dynamics Simulation, Macromolecules 39 (2006) 9630–9640.

[9] R. C. Rizzo, W. L. Jorgensen, OPLS All-Atom Model for Amines: Resolution of the Amine Hydration Problem, J. Am. Chem. Soc. 121 (1999) 4827–4836.